JOURNAL OF GEOPHYSICAL RESEARCH, VOL. 115, C12058, doi:10.1029/2009JC005665, 2010

Ocean wave spectrum properties as derived from quasi-exact computations of nonlinear wave-wave interactions

E. Gagnaire-Renou,[1,2,3] M. Benoit,[1,2] and P. Forget[3]

Received 27 July 2009; revised 15 December 2009; accepted 15 March 2010; published 11 December 2010.

[1] The estimation of nonlinear wave-wave interactions is one of the central problems in the development of operational and research models for ocean wave prediction. In this paper, we present results obtained with a numerical model based on a quasi-exact computation of the nonlinear wave-wave interactions called the Gaussian quadrature method (GQM) that gives both precise and computationally efficient calculations of the four-wave interactions. Two situations are presented: a purely nonlinear evolution of the spectrum and a duration-limited case. Properties of the directional wave spectrum obtained using GQM and the Discrete Interaction Approximation Method (DIM) are compared. Different expressions for the wind input and dissipation terms are considered. Our results are consistent with theoretical predictions. In particular, they reproduce the self-similar evolution of the spectrum. The bimodality of the directional distribution of the spectrum at frequencies lower and greater than the peak frequency is shown to be a strong feature of the sea states, which is consistent with high-resolution field measurements. Results show that nonlinear interactions constitute the key mechanism responsible for bimodality, but forcing terms also have a quantitative effect on the directional distribution of the spectrum. The influence of wind and dissipation parameterizations on the high-frequency shape of the spectrum is also highlighted. The imposition of a parametric high-frequency tail has a significant effect not only on the high-frequency shape of the spectrum but also on the energy level and peak period and on the global directional distribution.

Citation: Gagnaire-Renou, E., M. Benoit, and P. Forget (2010), Ocean wave spectrum properties as derived from quasi-exact computations of nonlinear wave-wave interactions, *J. Geophys. Res., 115,* C12058, doi:10.1029/2009JC005665.

1. Introduction

[2] Existing operational models for ocean wave modeling (either hindcasting or forecasting) are based on a transport equation for the wave action density. Since the pioneering model of *Gelci et al.* [1957], the understanding and modeling of surface wave dynamics has been constantly improving. The first models relied on parameterizations of the shape of the spectrum and/or of the physical processes [*Komen et al.*, 1994; *Young*, 1999; *Cavaleri et al.*, 2007; *Holthuijsen*, 2007]. About 20 years ago the first third-generation (3G) model, called WAM, was proposed by the *WAMDI Group* [1988]. Other 3G models have been developed in recent years, for example, WAVEWATCH [*Tolman*, 1991, 2002], Simulating WAves Nearshore [SWAN; *Booij et al.*, 1999], and TOMAWAC [*Benoit et al.*, 1996].

[3] These 3G discrete spectral models compute the evolution of the wave action density N, defined as $N(\mathbf{k}) = F(\mathbf{k})/\sigma$, where $F(\mathbf{k})$ is the directional (two-dimensional) variance spectrum of ocean waves, expressed here as a function of the wave number vector $\mathbf{k} = (k_x, k_y)$, and σ is the intrinsic wave frequency. This evolution can be described by the action balance equation, called the kinetic equation (KE), written for the general case of waves propagating in a medium with an ambiant current $\mathbf{U}$ as [e.g., *Phillips*, 1977; *Andrews and McIntyre*, 1978; *Komen et al.*, 1994]

$$\frac{\partial N}{\partial t} + \frac{\partial(\dot{x}N)}{\partial x} + \frac{\partial(\dot{y}N)}{\partial y} + \frac{\partial(\dot{k}_x N)}{\partial k_x} + \frac{\partial(\dot{k}_y N)}{\partial k_y} = Q(k_x, k_y, x, y, t), \tag{1}$$

with $\dot{x} = \partial\omega/\partial k_x$, $\dot{y} = \partial\omega/\partial k_y$, $\dot{k}_x = -\partial\omega/\partial x$, $\dot{k}_y = -\partial\omega/\partial y$, and $\omega = \sigma + \mathbf{k} \cdot \mathbf{U}$.

[4] The term Q on the right-hand side of equation (1) gathers the various source, sink, and transfer terms representing physical processes such as wind-wave interactions, wave-wave interactions, and dissipation of energy due to breaking, bottom friction, etc. In the present work, we assume that there is no ambient current and we limit our-

[1]Saint-Venant Laboratory for Hydraulics, Université Paris Est (Joint Research Unit EDF R&D/CETMEF/Ecole des Ponts ParisTech), Chatou, France.
[2]EDF R&D, Laboratoire National d'Hydraulique et Environnement, Chatou, France.
[3]Laboratoire de Sondages Electromagnétiques de l'Environnement Terrestre, CNRS UMR 6017, Sud Toulon Var University, La Garde, France.

0148-0227/10/2009JC005665

selves to deepwater conditions and spatially homogeneous cases; that is, we only consider the evolution in time. Equation (1) can then be simplified in the following way:

$$\frac{\partial N}{\partial t} = Q_{\mathrm{in}} + Q_{\mathrm{wc}} + Q_{\mathrm{nl4}}, \qquad (2)$$

where Q_{in} represents the energy input from the wind, Q_{wc} the dissipation by whitecapping, and Q_{nl4} the nonlinear four-wave interactions. Several models have been proposed during the past decades for Q_{in} and Q_{wc} [see, e.g., *Cavaleri et al.*, 2007]. Because the physics of wind-wave interactions and dissipation is quite complex and still only partially understood, the formulations used in existing 3G models involve some level of parameterization of the processes based on measurements and/or theoretical considerations. For the Q_{nl4} term a theoretical model has existed since the works by *Hasselmann* [1962] and *Zakharov* [1968] (see section 2). Existence of third-order nonlinear wave-wave interactions was confirmed experimentally by *McGoldrick et al.* [1966]. Recent efforts to validate and compare the theories of *Hasselmann* [1962] and *Zakharov* [1968] were undertaken by *Tanaka* [2001] and *Korotkevich et al.* [2008]. Many studies have already shown the importance of the Q_{nl4} term for proper modeling of the spectrum evolution, [e.g., *Young and Van Vledder*, 1993]. However, the complexity of Q_{nl4} makes its numerical computation time consuming, even using recent computers [*Cavaleri et al.*, 2007; *Janssen*, 2004]. In the mid-1980s, *Hasselmann et al.* [1985] developed an approximate computational method that was fast enough to be implemented in 3G operational models: Discrete Interaction Approximation (DIA). Improvements of DIA or alternative techniques were developed thereafter, mainly the multiple DIA method [*Van Vledder et al.*, 2000; *Tolman*, 2004] or more exact techniques such as EXACT-NL [*Hasselmann and Hasselmann*, 1981], the Webb-Resio-Tracy (WRT) method [*Webb*, 1978; *Resio and Perrie*, 1991], the Reduced Interaction Approximation Method (RIAM) [*Masuda*, 1980], and the Gaussian Quadrature Method (GQM) [*Lavrenov*, 2001]. Comparison between some of these methods can be found in the works of *Benoit* [2005] and *Cavaleri et al.* [2007]. A very recent approach, the two-scale approximation [*Resio and Perrie*, 2008], could also be promising, but further investigations are needed.

[5] This paper focuses on the effects of nonlinear wave-wave interactions on the structure of the wave spectrum. Our primary concern is to study the effect of a precise computation of the nonlinear term Q_{nl4} on the wave spectrum estimation. To that end we used a numerical algorithm adapted from the GQM proposed by *Lavrenov* [2001]. We addressed first the so-called conservative case, considering only the nonlinear transfer term in equation (2) ($Q_{\mathrm{in}} = Q_{\mathrm{wc}} = 0$), and then we addressed the simultaneous effects of the three physical processes of equation (2) by using existing models for Q_{in} and Q_{wc}. The temporal evolution of the spectrum and the structure of the directional distribution were analyzed.

[6] For the study of the dynamics of the wave spectrum evolution, we followed an approach similar to that of *Badulin et al.* [2005], who considered both the conservative case and the effects of wind input and dissipation. For a homogeneous and deep ocean, they showed that the conservative KE leads to self-similar solutions for the frequency spectrum [e.g., *Badulin et al.*, 2005; *Pushkarev et al.*, 2003]. These solutions are consistent with the theory of weak turbulence, leading to spectra of Kolmogorov type [*Zakharov and Filonenko*, 1966; *Zakharov and Zaslavsky*, 1982]. The shape and evolution of the directional spectrum was also simulated by *Lavrenov* [2003]. The wind input and dissipation were taken into account, for example, by *Banner and Young* [1994]. The nonstationary and nonhomogeneous equation was recently simulated by *Ardhuin et al.* [2007] using the WRT method. The finite depth case was investigated by *Polnikov* [1997] and *Resio et al.* [2001].

[7] We are particularly interested in the bimodality of the angular distribution of the wave spectrum (two peaks of the angular distribution at a given frequency) that is now known to occur at frequencies higher than the peak frequency and also in the low-frequency part of the spectrum. Indeed, until recently, the directional distribution of ocean waves had most often been considered unimodal. For instance, *Mitsuyasu et al.* [1975], *Hasselmann et al.* [1980], *Donelan et al.* [1985], *Elfouhaily et al.* [1997], and *Kudryavtsev et al.* [1999] provided unimodal parameterizations of the directional distribution. Remote-sensing measurements carried out with airborne radars or lidars, aerial stereo-photography techniques, HF radars, etc., evidenced bimodality in the directional spectrum of surface gravity waves (see *Hwang et al.*, 2000b, for a review). Bimodal directional distributions were also measured by directional buoys or arrays of wave gauges [*Young*, 1994; *Young et al.*, 1995; *Ewans*, 1998; *Wang and Hwang*, 2001; *Long and Resio*, 2007]. These data all show the bimodal structure of the angular distribution at frequencies higher than the spectral peak. These observations suggest that bimodality could be a fundamental feature of the wind-wave spectrum for very different water depth and wind conditions, which supports the idea that the nonlinear wave-wave interactions play an important role in the mechanism that creates and maintains bimodality [*Banner and Young*, 1994]. It should be noticed that bimodality associated with another mechanism (Phillips resonance mechanism of wind-wave generation) was observed using HF radars by *Trizna et al.* [1980].

[8] The organization of the paper is as follows. Section 2 introduces the basic equations and numerical methods for computing Q_{nl4}. Section 3 presents the simulation results of the conservative KE. (The model equation and initial conditions are given in section 3.1, the concept of self-similarity is discussed in section 3.2, and the evolution of representative sea state parameters, frequency spectrum, and directional distribution are analyzed in sections 3.3, 3.4, and 3.5 and 3.6, respectively). Section 4 describes the effects of wind input and dissipation by whitecapping. Section 5 gives our conclusions and perspectives for this work.

2. Equations and Numerical Methods

2.1. Nonlinear Four-Wave Interactions Q_{nl4}

[9] Third-generation spectral models aim at representing each physical process in a source term as reliably as possible. This is rather difficult, either because the physics is poorly understood, which is the case for the dissipation by whitecapping, or because the computational method is too time-consuming, which is the case for the nonlinear four-

wave interactions. Several models and parameterizations have been implemented for wind input and whitecapping dissipation. Regarding the term Q_{nl4}, a theoretical model has been available since the works of *Hasselmann* [1962] and *Zakharov* [1968], who independently formulated its expression as a Boltzmann-type integral:

$$Q_{nl4}(\mathbf{k}_1) = \int_{\mathbf{k}_2}\int_{\mathbf{k}_3}\int_{\mathbf{k}_4} G(\mathbf{k}_1,\mathbf{k}_2,\mathbf{k}_3,\mathbf{k}_4)\{N_3N_4(N_1+N_2) \\ -N_1N_2(N_3+N_4)\} \times \delta(\mathbf{k}_1+\mathbf{k}_2-\mathbf{k}_3-\mathbf{k}_4) \\ \cdot\,\delta(\sigma_1+\sigma_2-\sigma_3-\sigma_4)d\mathbf{k}_2 d\mathbf{k}_3 d\mathbf{k}_4. \quad (3)$$

[10] In the preceding expression, N_j stands for $N(\mathbf{k}_j)$ and σ_j is the frequency corresponding to the wave number k_j through the dispersion relationship ($\sigma^2 = gk$). $G(\mathbf{k}_1, \mathbf{k}_2, \mathbf{k}_3, \mathbf{k}_4)$ is the coupling coefficient, whose expression may be found in the work of *Webb* [1978], for instance. As indicated by the two Dirac δ functions, the interactions occur between quadruplets of spectral components that fulfill the two resonance conditions:

$$\begin{cases} \mathbf{k}_1+\mathbf{k}_2 = \mathbf{k}_3+\mathbf{k}_4, \\ \sigma_1+\sigma_2 = \sigma_3+\sigma_4. \end{cases} \quad (4)$$

[11] The computation of this complicated nonlinear six-fold integral is a tricky problem. The exact evaluation of equation (3) requires specific algorithms together with a large computational time, so in operational wave models this nonlinear term is most often evaluated by approximate and simplified methods. The most commonly used technique is DIA [*Hasselmann et al.*, 1985], which only considers a particular arrangement of wave components. In spite of its wide use, DIA suffers from a number of limitations [*Van Vledder et al.*, 2000]. *Benoit* [2005] compared several methods to evaluate the nonlinear interactions in deepwater conditions and highlighted significant differences between them. Only quasi-exact methods, such as those proposed by *Webb* [1978] or *Lavrenov* [2001], allow an accurate evaluation of this term.

[12] Therefore, our concern is to work on a method that can be suitable for use in operational models but that has a higher precision than DIA. In this perspective, we developed an efficient numerical algorithm to compute the Boltzmann integral, the GQM, on the basis of the work of *Lavrenov* [2001].

2.2. GQM Method

[13] The GQM is based on the use of Gaussian quadratures for the various numerical integrations in equation (3). The six-dimensional integral can be reduced to a three-dimensional integral over σ_2, θ_2, and σ_3 when suppressing the two Dirac resonance conditions. Indeed, the term $\delta(\mathbf{k}_1 + \mathbf{k}_2 - \mathbf{k}_3 - \mathbf{k}_4)$ involves $\mathbf{k}_4 = \mathbf{k}_1 + \mathbf{k}_2 - \mathbf{k}_3$, which permits elimination of two dimensions of integration. We chose to work with the spectrum $F(\sigma, \theta)$. The change of variable from $\mathbf{k}$ to (σ, θ) thus leads to an integral over σ_2, θ_2, σ_3, and θ_3. Then integration over θ_3 eliminates the second Dirac. Rewriting the equation in terms of the variance spectrum F (instead of the action density N), we obtain the following expression:

$$\frac{\partial F_1}{\partial t} = \int_{\sigma_2=0}^{+\infty}\int_{\theta_2=0}^{2\pi}\int_{\sigma_3=0}^{\sigma_a/2} 2\,\frac{\sigma_a^4 G}{\sigma_2\sigma_3\sigma_4} \\ \cdot\,\frac{F_3F_4\left(F_1\sigma_2^4+F_2\sigma_1^4\right)-F_1F_2\left(F_3\sigma_4^4+F_4\sigma_3^4\right)}{\sqrt{\tilde{B}_0(\varepsilon_a,w_3)\tilde{B}_1(\varepsilon_a,w_3)\tilde{B}_2(\varepsilon_a,w_3)}}d\sigma_2 d\theta_2 d\sigma_3, \quad (5)$$

where $\sigma_a = \sigma_1 + \sigma_2 = \sigma_3 + \sigma_4$, $\varepsilon_a = 2gk_a/\sigma_a^2$ with $\mathbf{k}_a = \mathbf{k}_1 + \mathbf{k}_2 = \mathbf{k}_3 + \mathbf{k}_4$, $w_3 = \sigma_3/\sigma_a$, and $\tilde{B}_0$, $\tilde{B}_1$, and $\tilde{B}_2$ are three nondimensional functions.

[14] The integration over θ_3 introduces singularities because the denominator of equation (5) can be equal to zero. The specificity of the GQM, which makes it an optimal algorithm of integration, is the use of quadratures adapted to these singularities. Integration over σ_3 is divided into two intervals and computed with Gauss-Legendre and Gauss-Chebyshev quadratures. Integration over θ_2 uses Gauss-Chebyshev quadrature and the last integration (over σ_2) is performed with a simple trapezoidal method.

[15] The GQM can be used with a reduced number of integration points in the quadrature formulas, plus some filtering to discard configurations that have negligible or minor contributions to the overall integral. Thus, the computing time can be reduced, while the method still produces results with high accuracy.

[16] To study the properties and the robustness of our algorithm, we performed simulations with different resolutions of the method, i.e., different numbers of points for the numerical integration. Three resolutions were tested by *Benoit and Gagnaire-Renou* [2007], a "fine" resolution (26 points for the integration on σ_2, 16 points for the integration on θ_2, and 12 points for the integration on σ_3), a "medium" resolution (14, 8, and 8), and a "rough" resolution (11, 6, and 6). To illustrate the performance of the GQM, we present in Figure 1 the (angular integrated) nonlinear transfer terms Q_{nl4} as obtained with various methods. The nonlinear terms are computed for a directional wave spectrum corresponding to case 3 in the work of *Hasselmann et al.* [1973], which combines a Joint North Sea Wave Project (JONSWAP) frequency spectrum $E(f)$ with Phillips constant $\alpha = 0.01$, peak frequency $f_p = 0.3$ Hz, peak enhancement factor $\gamma = 3.3$, $\sigma = 0.07$ if $f \leq f_p$ and $\sigma = 0.09$ if $f > f_p$, and a frequency-independent angular spreading function $D(\theta) = \Delta\cos^4(\theta)$ over $[-\pi/2, \pi/2]$. It can been seen from Figure 1 that the Q_{nl4} term computed with the fine-resolution GQM is very close to the term computed by the EXACT-NL code by *Hasselmann and Hasselmann* [1981], although this latter term exhibits some spurious oscillations. Results obtained with the rough-resolution GQM are a bit more irregular than those obtained with the fine-resolution GQM but are in very good overall agreement. In comparison, it is seen that the Q_{nl4} term computed with the DIA method is clearly different, both in magnitude and in the shape of the lobes of the nonlinear transfer term. The fine and medium resolutions give almost identical results (not shown in Figure 1 because

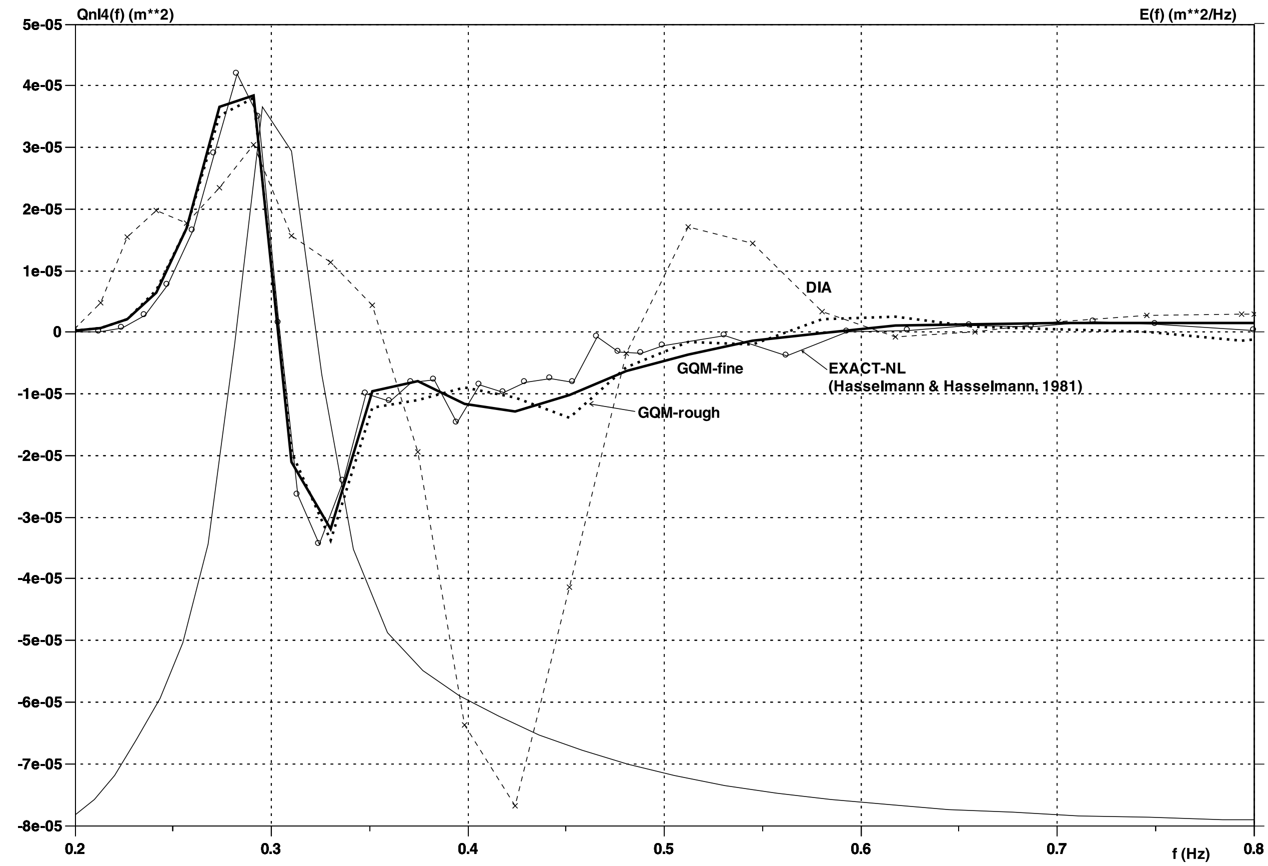

Figure 1. Angular integrated nonlinear transfer terms $Q_{nl4}(f)$ computed with various methods: EXACT-NL, DIA, GQM-fine, and GQM-rough for the spectrum of case 3 of [*Hasselmann and Hasselmann*, 1981]. The frequency spectrum $E(f)$ is superimposed.

the curves are very close). Comparison of results thus confirmed the good convergence of the method when increasing its resolution.

[17] The choice of the optimum setting for practical applications requires that the computing time be taken into account. For simulation of the conservative KE, the medium resolution requires 3–4 times more CPU time than the rough resolution, and the fine calculation requires 25 times more CPU time than the rough one. In comparison with DIA, the rough resolution is 80 to 100 times slower. This can be compared with the CPU times of the EXACT-NL code (approximately 1000 times DIA) and the WRT method (approximately 300 times DIA). Therefore, the method appears suitable for implementation in 3G models. In the remainder of this paper, simulations are handled using the GQM with medium resolution. Results obtained using the GQM (medium) and the DIA methods are compared throughout the paper.

2.3. Numerical Aspects

[18] It should first be recalled that numerical settings (e.g., spectral resolution and range, time step, diagnostic tail, and growth limiter) cannot be dissociated from the parameterizations of the physical processes themselves [e.g., *Tolman*, 1992]. Here the time integration of the source terms in equation (2) is performed using a semi-implicit scheme with a dynamic time step. This time step is calculated at each iteration so that the relative variation of the variance spectrum as the result of the input, dissipation, and transfer terms during a time step remains below a threshold ε (generally 5–10%). No wave growth limiter is used in these simulations.

[19] For some calculations (set III-it in section 4), a diagnostic tail (or constrained tail) is applied to the spectrum above $f_d = \min[f_{max}; \max(4f_{PM}, 2.5f_{mean})]$, where f_{max} is the last discrete frequency, f_{PM} is the Pierson-Moskovitz frequency, and f_{mean} is the mean frequency. It means that the high-frequency range of the spectrum is constrained to decrease as f^{-m} with m a fixed parameter, called the "tail factor," set to $m = 4$ in our simulations.

[20] In the following, the high-frequency shape of the spectrum is often called the HF tail. The implications of imposing a f^{-4} HF tail is discussed later in the paper.

[21] No diagnostic tail is applied for the simulations of sections 3 and 4 (sets I, II, and III-ft). However, above the last discrete frequency f_{max}, the spectrum is assumed to have an f^{-4} shape.

3. Results for the Conservative Equation (No Wind Input or Dissipation)

3.1. Model Equation and Initial Conditions

[22] We first address the particular case of the evolution of ocean waves when there is no energy input from the wind or

Table 1. Description of the Initial Spectra: Cases C1–C4

Initial Case	Description of spectra $F(f, \theta) = E(f)D(\theta)$	a (H_{m0} = 0.05 m)	b (H_{m0} = 0.10 m)
C1	$E(f)$: step, $D(\theta)$: half plane $E(f) = A$ ($0.8 \leq f \leq 1.2$ Hz), $E(f) = 0$ (otherwise) $D(\theta) = 1/\pi$ ($90° \leq \theta \leq 270°$), $D(\theta) = 0$ (otherwise)	$A = 3.91 \times 10^{-4}$	$A = 1.56 \times 10^{-3}$
C2	$E(f)$: Gaussian, $D(\theta)$: half plane $E(f) = A\ \exp[-\frac{(f-f_p)^2}{2\sigma^2}$, $f_p = 1$ Hz, $\sigma = 0.1$	$A = 6.23 \times 10^{-4}$	$A = 2.49 \times 10^{-3}$
C3	$E(f)$: JONSWAP, $D(\theta)$: broad cardioid $E(f) = Ag^2(2\pi)^{-4} f^{-5} \exp\left[-\frac{5}{4}\left(\frac{f}{f_p}\right)^{-4}\right]\gamma^{\exp\left[-\frac{(f-f_p)^2}{2\sigma^2 f_p^2}\right]}$ $f_p = 1$ Hz, $\sigma = 0.07$ if $f \leq f_p$, $\sigma = 0.09$ if $f > f_p$, $\gamma = 3.0$ $D(\theta) = 0.51 \cos^6\left[\frac{1}{2}(\theta - \theta_0\right]$, $\theta_0 = 180°$	$A = 8.62 \times 10^{-3}$	$A = 3.45 \times 10^{-2}$
C4	$E(f)$: JONSWAP, $D(\theta)$: narrow cardioid $D(\theta) = 1.27 \cos^{40}\left[\frac{1}{2}(\theta - \theta_0)\right]$, $\theta_0 = 180°$	$A = 8.62 \times 10^{-3}$	$A = 3.45 \times 10^{-2}$

dissipation. In this case, equation (2), written in terms of the variance spectrum F, reduces to

$$\frac{\partial F}{\partial t} = Q_{\mathrm{nl4}}. \tag{6}$$

[23] We performed several runs to investigate the effect of the initial energy and wave steepness, and of the initial shape of the spectrum, on the evolution of F. This latter effect is written as $F(f, \theta) = E(f)D(f, \theta)$, with θ the wave direction, F the frequency (one-dimensional) variance spectrum, and D the directional spreading function satisfying $\int_\theta \mathrm{D}(f, \theta) = 1$.

[24] The wave (total) energy is $E_{\mathrm{tot}} = \rho g \int_f E(f)df$, with g the gravitational acceleration and ρ the seawater density. The spectral significant wave height is defined as $H_{m0} = 4\sqrt{m_0}$, with m_0 the zero-order moment of $E(f)$. The spectral peak frequency, f_p, is another important parameter. The wave steepness is defined here as $\varepsilon = k_p H_{m0}/2$, with $k_p = (2\pi f_p)^2/g$.

[25] The initial peak frequency f_{p0} was always fixed to 1 Hz. Eight cases were considered, corresponding to four initial shapes of F (labeled C1 through C4), combined with two values of initial H_{m0} (labeled a and b): 0.05 and 0.10 m (the corresponding steepnesses are 0.10 and 0.20, respectively).

[26] The parameters defining the initial spectra are given in Table 1. The different shapes for $E(f)$ and $D(\theta)$ are illustrated in Figure 2. Cases C1 and C2 were chosen to examine how the model responds when a nonrealistic spectrum is imposed at the beginning of the run.

[27] The discrete grid is composed of 128 frequencies, with geometric spacing ($f_{i+1}/f_i = 1.024$) from $f_{p0}/5$ (0.2 Hz) to $4f_{p0}$ (4 Hz) and 72 directions with a constant spacing of 5°. The simulations were run during 128 h of physical time.

[28] Simulations were computed using the GQM. To compare with the DIA method, we repeated the same simulations by simply replacing GQM by DIA in equation (6), parameters and computing options being identical for both methods.

3.2. Concept of Self-Similarity

[29] The self-similar solutions of the conservative homogeneous KE [equation (6)], called "purely nonlinear" KE, can be written as [*Pushkarev et al.*, 2003; *Badulin et al.*, 2005]

$$N(\mathbf{k}, t) = at^{\alpha} U_{\beta}(\xi), \xi = b\mathbf{k}t^{\beta}, \tag{7}$$

where U_β is a shape function and a, α, b, and β are constants. Values of α and β are 4/11 and 2/11, respectively.

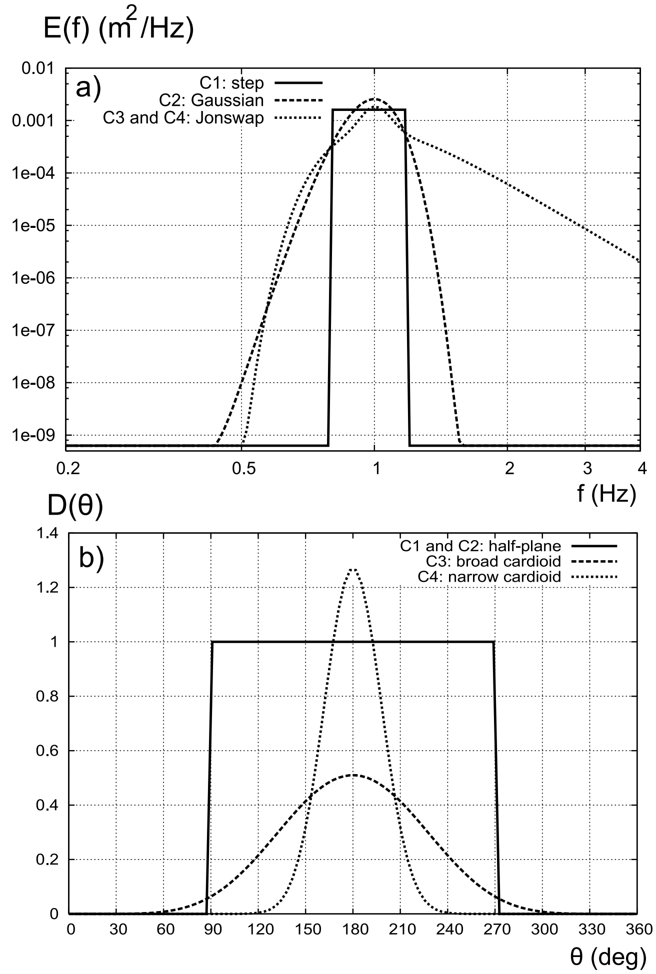

Figure 2. Initial conditions: (a) three different frequency spectra (step, Gaussian, and JONSWAP) combined with (b) three different distributions $D(\theta)$ (half plane, and broad and narrow cardioids).

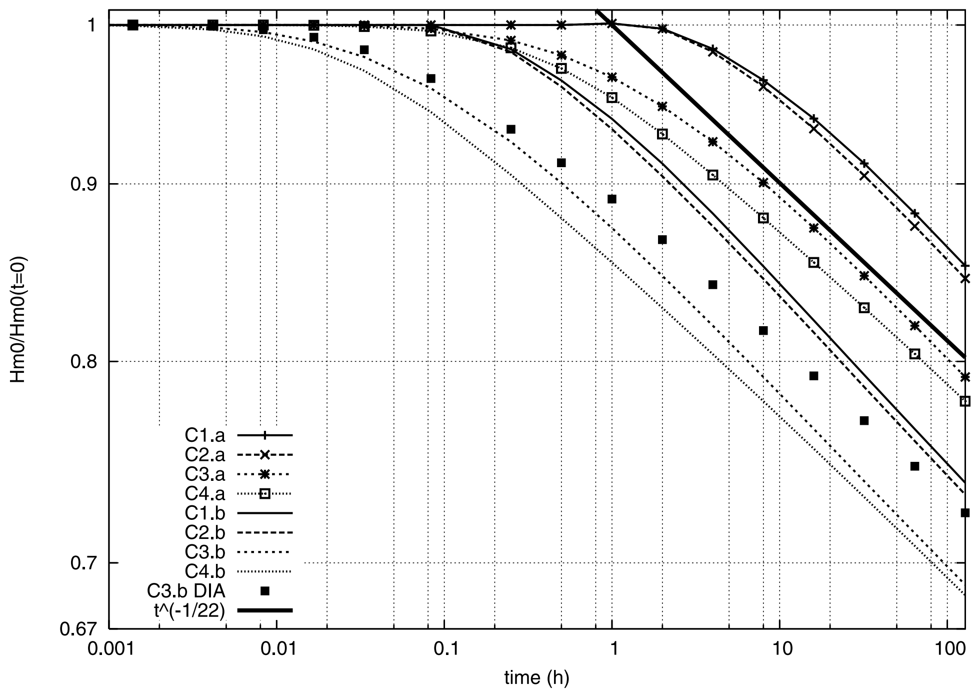

Figure 3. Time evolution of $H_{m0}/H_{m0,\mathrm{init}}$: GQM, eight test cases; DIA, case C3.b. Comparison to the law in $t^{-1/22}$ [*Badulin et al.*, 2005].

[30] The variance spectrum is written as

$$F(\sigma,\theta,t) = a^{'} t^{\alpha} \sigma^4 U_{\beta}(y,\theta), y = b^{'} \sigma^2 t^{\beta}, \tag{8}$$

where a′ and b′ are constants.

[31] Spectra that are the solution of equation (6) have a strong tendency toward self-similar behavior. This means that the shape function U_β becomes time-independent after a short simulation time.

[32] One can deduce from these solutions that the total energy E_{tot} decreases as $t^{-1/11}$ [*Pushkarev et al.*, 2003; *Badulin et al.*, 2005], which leads to $H_{m0} \propto t^{-1/22}$. The self-similar solutions also describe the downshift of the spectral peak frequency f_p, varying as $t^{-1/11}$. These results are assessed in the following.

3.3. Evolution of Representative Sea State Parameters

[33] Figure 3 shows the time evolution of $H_{m0}/H_{m0,\mathrm{init}} = H_{m0}/H_{m0}$ (t = 0) using the GQM algorithm. This evolution is compared with $t^{-1/22}$ and with the $H_{m0}/H_{m0},_{\mathrm{init}}$ curve obtained with the DIA method for C3.b.

[34] The value of H_{m0} is monotonically decreasing, which means that the energy is not conserved. There is a loss of energy with time because the integration of the KE is performed over a limited frequency domain (0.2–4 Hz) and the nonlinear wave interactions carry part of the energy out of this range. After a certain time, H_{m0} evolves like $t^{-1/22}$. As energy is proportional to H_{m0}^2, we verify the behavior of E_{tot} in $t^{-1/11}$ (described by, e.g., *Badulin et al.* [2005]). This confirms the known theoretical result that the wave energy is only formally conserved [*Pushkarev and Zakharov*, 2000; *Pushkarev et al.*, 2003].

[35] We note that H_{m0} begins to behave like $t^{-1/22}$ more rapidly for C3 and C4 than for C1 and C2. Indeed, with the initial step-like or Gaussian spectra (C1 and C2), H_{m0} is conserved over the modeled frequency range until the HF part of the spectrum reaches the upper frequency f_{max}; then energy starts leaking toward higher frequencies. As pointed out by *Young and Van Vledder* [1993] and *Young* [1999], even if the nonlinear interactions can involve components of the whole wave number space, they are much more effective for neighboring than for distant components. Thus, losses of energy at high frequencies are small when the high-frequency energy level is low, as in cases C1 and C2 where a small amount of energy is sent outside the discretization domain at the beginning of the simulation. The initial JONSWAP-type spectra (C3 and C4) start leaking toward higher frequencies from the beginning of the simulation because of their initial f^{-5} high-frequency shape. Furthermore, H_{m0} evolution for the step-like and Gaussian cases (C1 and C2) is very similar, which shows that, apart from the effect of the HF shape, the initial shape of $E(f)$ has a small influence. The initial angular distribution $D(\theta)$ does not affect the evolution of H_{m0} as seen on C3 and C4 curves that are very similar.

[36] The time evolution of $H_{m0}/H_{m0,\mathrm{init}}$ depends on the initial value of H_{m0} or the corresponding initial steepness ε: it is faster when $\varepsilon_{\mathrm{init}}$ is larger. This is caused by more intense nonlinear energy transfers as the steepness of the sea state increases. In case a ($\varepsilon_{\mathrm{init}}$ = 0.10), H_{m0} is reduced by 15–20% at the end of the simulation. In case b ($\varepsilon_{\mathrm{init}}$ = 0.20), the decrease is larger, about 25–30%.

[37] The DIA curve shows a smaller decrease than the GQM curve for the same case (C3.b), which may be related

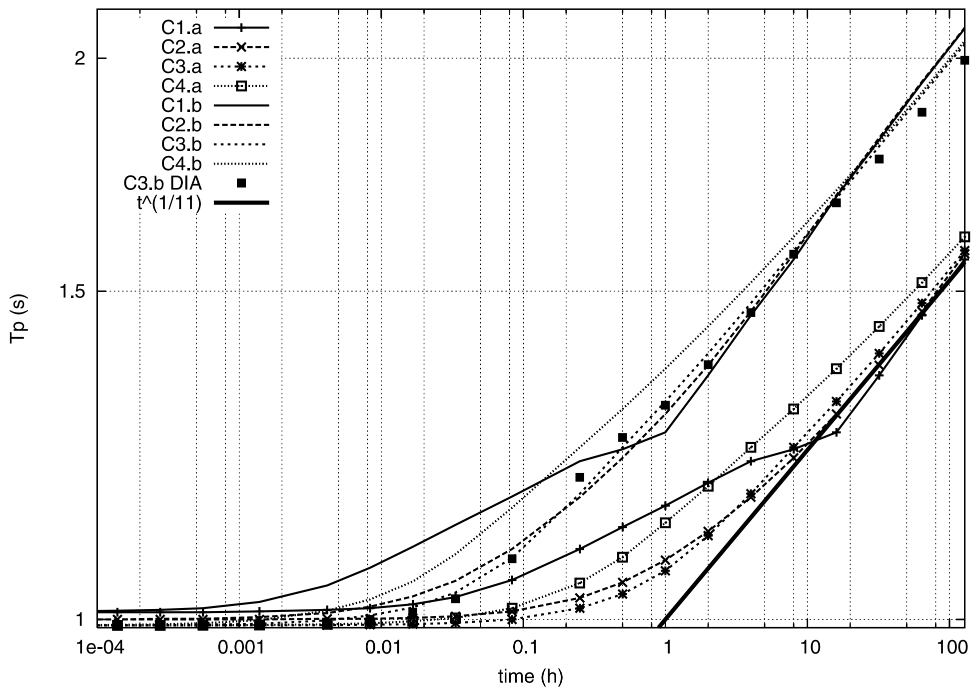

Figure 4. Time evolution of the peak period of the wave spectrum T_p: GQM method, eight test cases; DIA, case C3.b. Comparison to the law in $t^{1/11}$ [*Badulin et al.*, 2005].

to the slower formation of the HF tail when using DIA (see section 3.4).

[38] Another important parameter to look at is the peak period T_p (Figure 4). Results obtained with the same initial steepness are quite close to each other, suggesting that the influence of the initial shape of the directional spectrum is weak. By contrast, the influence of the initial steepness is more significant: T_p varies more rapidly for a larger $\varepsilon_{\rm init}$ and increases to a much higher value. This reflects that the spectrum migrates faster toward low frequencies. Further-

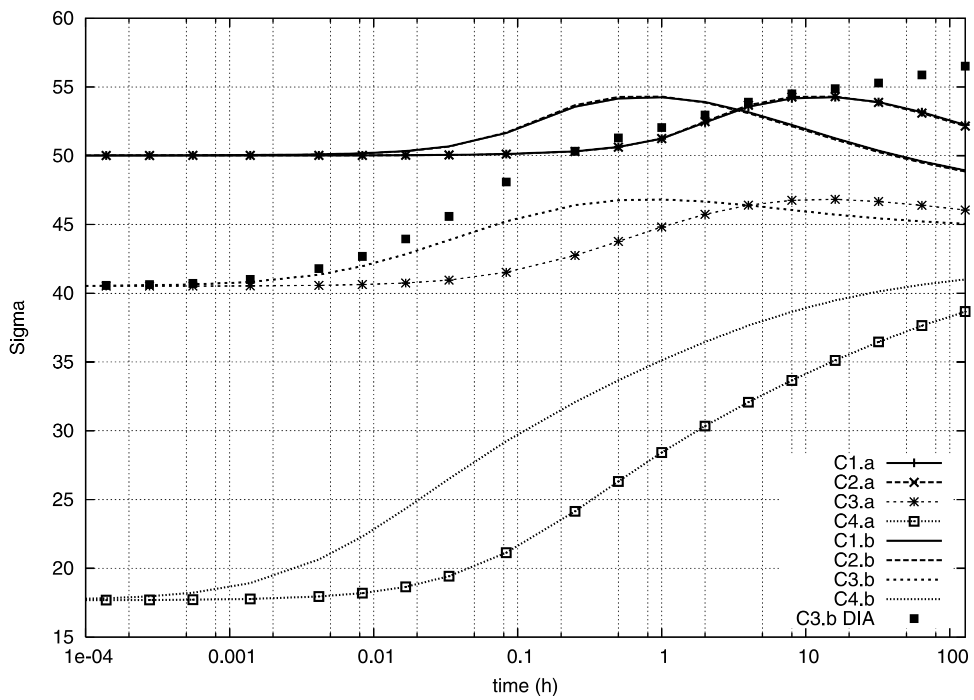

Figure 5. Time evolution of the wave spectrum mean angular width σ. GQM method, eight test cases; DIA, case C3.b.

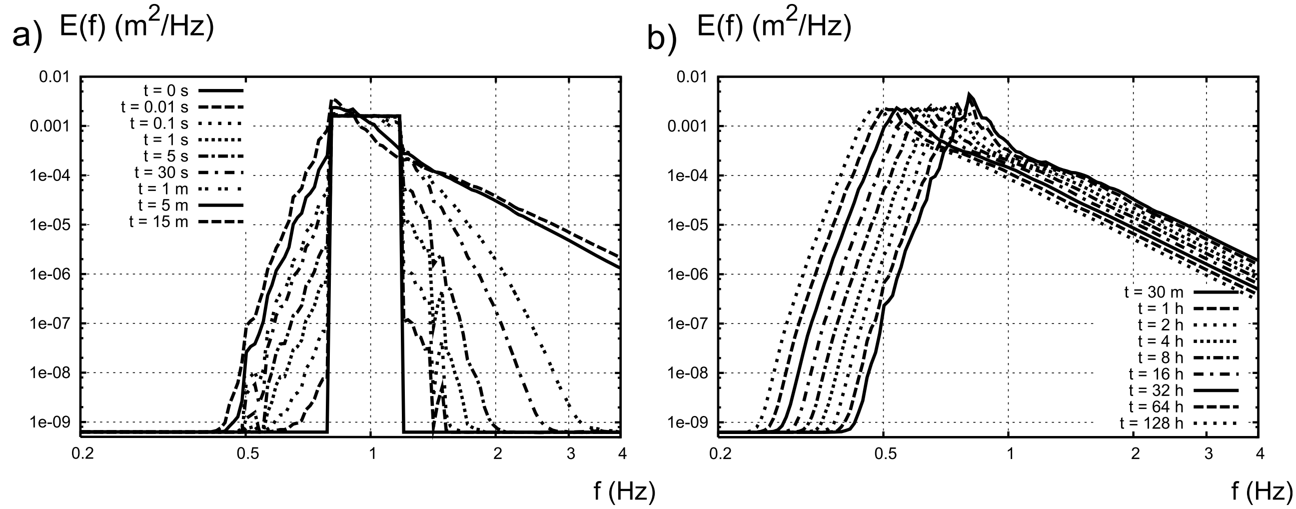

Figure 6. Evolution of the frequency spectrum $E(f)$ (from 0 to 128 h), using the GQM, for the initial case C1.b: (a) short-term evolution (from 0 to 15 min) and (b) long-term evolution (from 30 min to 128 h).

more, it can be noticed that, after a certain time, T_p tends to vary in $t^{1/11}$. This reproduces the downshift of the spectral peak according to the self-similarity theory [*Pushkarev et al.*, 2003; *Badulin et al.*, 2005]. Comparisons with DIA results show small differences.

[39] Finally, we examine the mean angular width defined by

$$\sigma = \frac{\int_f \sigma(f)E(f)df}{\int_f E(f)df},$$

with $\sigma(f) = \sqrt{2(1-m_1)}$ and $m_1 = \int_0^{2\pi} D(f,\theta)\cos(\theta-\theta_0)d\theta$, where $\theta_0(f)$ is the mean direction of the wave field (Figure 5). σ converges to a value in the range 40–50° depending on the initial conditions. The time evolution of σ for cases C1 and C2 (same initial angular half plane distribution) is identical. The two other cases (cardioids) evolve in a quite different way. The initial value of σ for C4 [$\cos^{40}(\theta/2)$ initial angular distribution] is smaller than the other ones. Thus, σ monotonically increases during the simulation. For cases C1–C3, σ starts increasing at the beginning of the simulation and then decreases. Differences between cases C*i*.a and C*i*.b can be noticed: the mean angular width appears to be changing much more quickly in case b (higher initial steepness). DIA simulations give a much higher σ, increasing with time.

3.4. Evolution of the Frequency Spectrum

[40] Results using GQM (Figures 6 and 7) and DIA (Figures 8 and 9) algorithms for evaluating Q_{nl4} are consecutively presented. Figure 6 reports the temporal evolution of $E(f)$ for case C1.b. A short-term scale of 0 to 15 min (Figure 6a) and a long-term scale of 30 min to 128 h (Figure 6b) are considered. The beginning of the simulation is a period of intense wave-wave energy transfers. During this phase, the spectrum, which presents a shape very different from the quasi-equilibrium final shape, evolves very rapidly. A main peak appears after about 15 min and then migrates toward lower frequencies. The high-frequency (often referred to as HF) part of the spectrum takes a typical shape in f^{-m} with $m \approx 4.1$ after a short time period ($t \geq$ 15 min).

[41] The spectra of the eight cases considered (not shown) evolve similarly with time. The shape of $E(f)$ reached at the end of the simulations slightly depends on the initial shape. The time evolution of $E(f)$ is faster for larger (cases C*i*.b) than for smaller ε_{init} (cases C*i*.a).

[42] To verify the self-similar evolution of the spectrum (section 3.2), Figure 7 shows the shape function U_β for a wave direction corresponding to the main direction of propagation (θ_0 = 180°) superimposed at seven times, spanning the interval 2–128 h (case C3.b). The variations of U_β during this interval are very small (less than a few percent), which confirms a self-similar evolution. Cases C1.b,

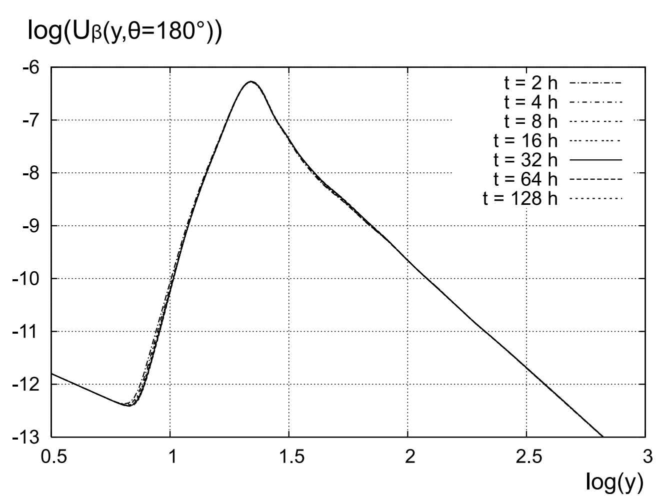

Figure 7. Variation of the shape function $U_\beta(y, \theta = 180°)$ with y [equation (8)], as computed using the GQM between t = 2 h and t = 128 h. Initial spectrum is case C3.b.

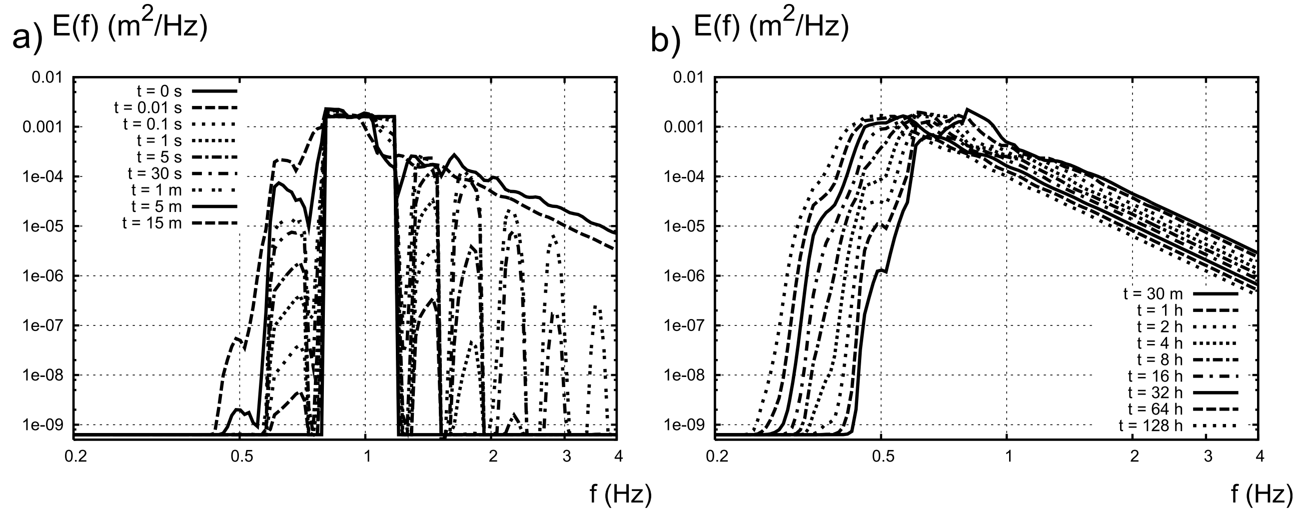

Figure 8. Time evolution of the frequency spectrum, using the DIA method for the initial case C1.b: (a) short-term evolution (from 0 to 15 min) and (b) long-term evolution (from 30 min to 128 h).

C2.b, and C4.b also lead to self-similarity after a few hours (not shown).

[43] On the whole, the self-similarity depends little on the initial spectrum. The time necessary to reach self-similarity depends on the initial steepness. Indeed, in the cases C*i*.a, the spectrum needs more time (about 16–32 h) to reach its typical self-similar shape.

[44] These results show that the dynamical evolution of the spectrum is described in an almost perfect way by the self-similarity equations (7) and (8). Moreover, they confirm the ability of our algorithm to reproduce the expected theoretical evolution.

[45] The DIA spectra obtained in the same conditions (Figure 8) are quite different from the GQM spectra, especially at the beginning of the simulation (t < 5 min), for frequencies greater than the peak frequency. Instead of an f^{-4} tail, the DIA method produces a succession of peaks in the HF range. However, after some time (about 5 min), we also observe with DIA the formation of the f^{-4} HF tail. At the end of the simulation, the DIA spectrum has a larger bandwidth than the GQM spectrum, and its peak value is lower. The self-similarity of DIA frequency spectrum is shown in Figure 9 (case C3.b). As for the GQM simulations, the self-similarity of $E(f)$ is observed after a few hours (depending on the initial case). This is not surprising because the collision integral Q_{nl4} [equation (3)] obeys homogeneity properties [*Badulin et al.*, 2005] for both methods of calculation of the nonlinear interactions. Self-similar solutions can thus be derived in both cases.

3.5. Angular Spreading of Wave Energy

[46] Here we aim at analyzing the detailed angular distribution of energy. To that end, we computed the normalized directional spreading function under the form $\tilde{D}(f/f_p, \theta) = D(f/f_p, \theta)/D_{max}(f/f_p)$, where $D_{max}(f/f_p)$ is the maximum value of $D(f/f_p, \theta)$ over θ at each frequency f/f_p.

[47] The function $\tilde{D}(f/f_p, \theta)$ is represented for GQM in Figure 10a at t = 128 h for case C2.b. This representation allows us to get a better idea of the structure of the directional distribution, although the normalized values at each frequency can give some false impressions. In particular, we should remember that at high frequencies the absolute values of the spectrum are low and that the HF bimodality is somewhat amplified by this normalization. The GQM clearly exhibits the bimodal structure of the angular distribution for frequencies above and below the peak frequency. The side lobes are symmetrically placed around the mean direction θ_0 = 180°. The directional distribution is unimodal and very narrow near the peak frequency. For $f/f_p \geq 4$, the directional spectrum becomes unimodal again but is much more isotropic. This structure is caused by nonlinear interactions that redistribute energy to large angles from the mean wave direction and contribute to the broadening of the spectrum [*Young and Van Vledder*, 1993]. Figure 11 illustrates these redistributions of energy rather well. It shows that Q_{nl4} sends energy in oblique directions, not only at frequencies

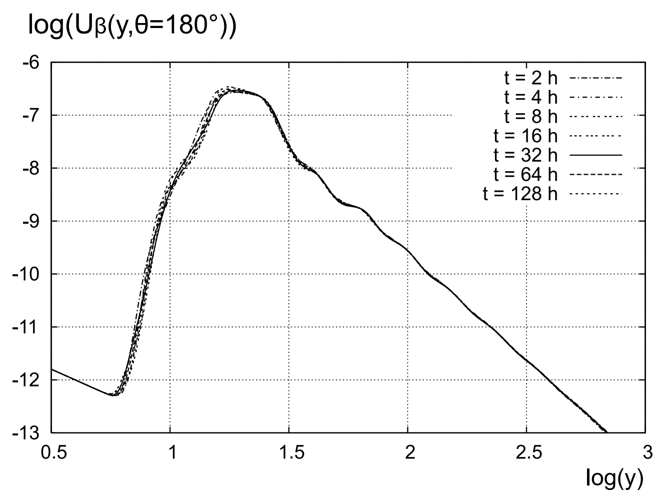

Figure 9. Variation of the shape function $U_\beta(y, \theta = 180°)$ with y [equation (8)], as computed using DIA between t = 2 h and t = 128 h. Initial spectrum is case C3.b.

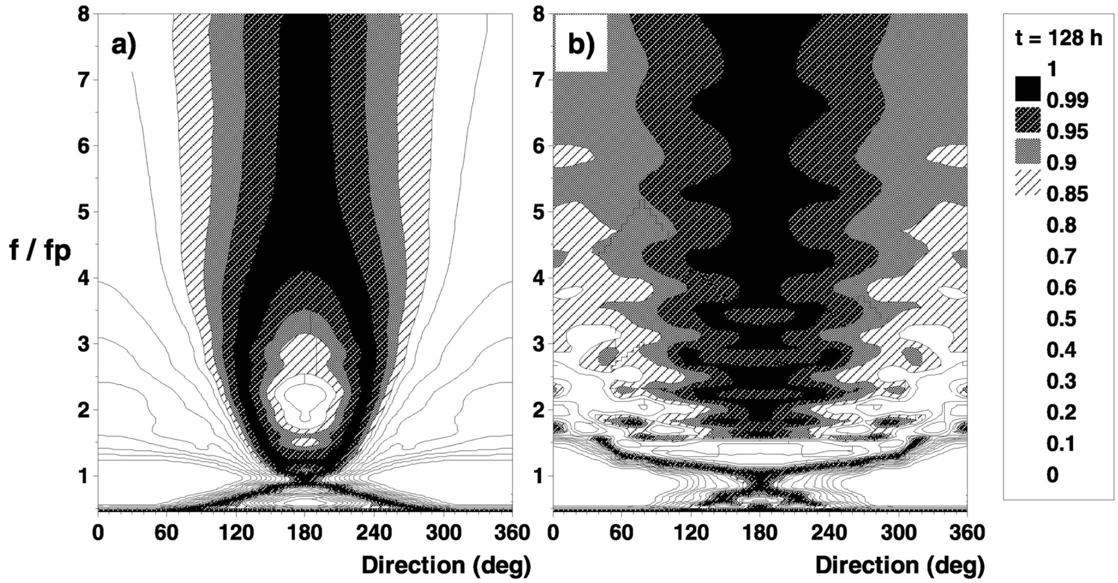

Figure 10. Normalized directional spreading function $\tilde{D}(f/f_p, \theta)$ at t = 128 h, case C2.b: (a) GQM and (b) DIA method.

above the peak but also at low frequencies (Figure 11b), and induces the relatively narrow distribution of the spectrum around the peak. The unimodality of the directional distribution for frequencies above $4f_p$ could be explained by the weakness of the Q_{nl4} term at these frequencies at the end of the simulation, which is too small to redistribute energy to oblique directions.

[48] The variation of the angle between the two (symmetric) lobes, $2\theta_l$ (where θ_l is the angle between each lobe and the main direction), with f/f_p is shown in Figure 12. For frequencies greater than f_p, $2\theta_l$ increases to a maximum varying in the range 110–140°. This maximum is reached for frequencies between $2f_p$ and $3f_p$. Then $2\theta_l$ decreases and the directional spectrum becomes unimodal for frequencies between 3.8 and $6f_p$.

[49] Figure 10b represents $\tilde{D}(f/f_p, \theta)$ obtained using DIA, again at t = 128 h for case C2.b. The results are dramatically different. The directional distribution is very irregular. Nevertheless, we can note that the two distributions are unimodal and narrow near the peak frequency and seem to be bimodal below f_p.

[50] Figure 13 compares sections of $D(f, \theta)$ at different frequencies for GQM and DIA simulations (initial case C3. b). The shape of the directional distribution obtained using

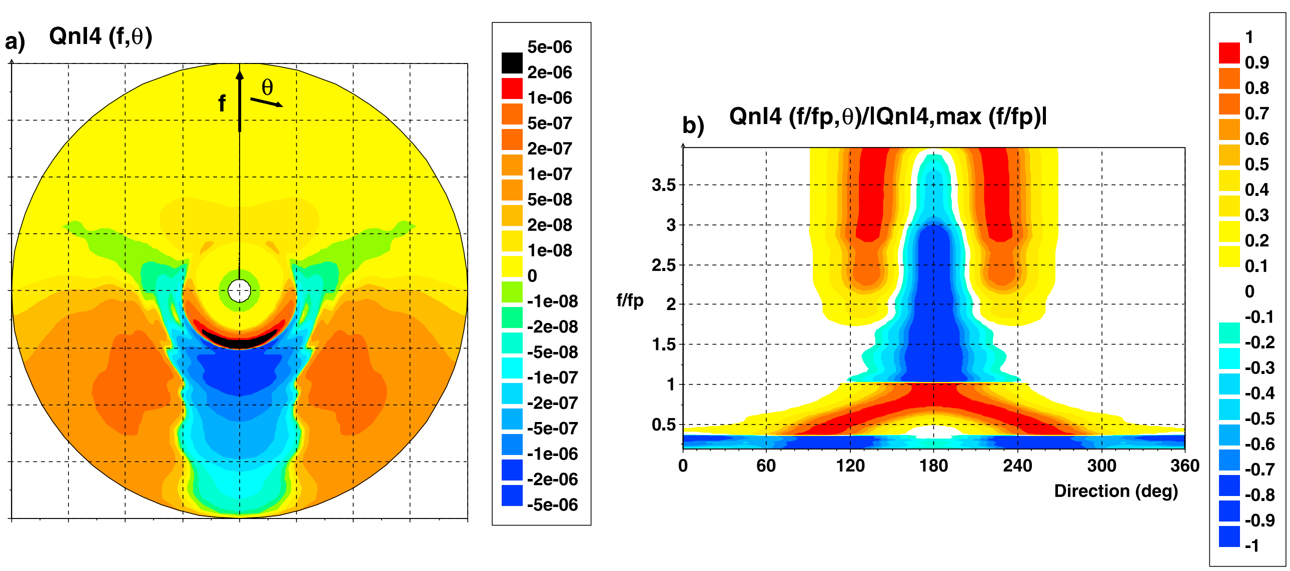

Figure 11. Nonlinear transfer term Q_{nl4} calculated by the GQM at t = 0.01 s (first time step) for case C3. b: (a) $Q_{\mathrm{nl4}}(f, \theta)$ in polar coordinates and (b) $Q_{\mathrm{nl4}}(f/f_p, \theta)/|Q_{nl4,\max}(f/f_p)|$ in Cartesian coordinates.

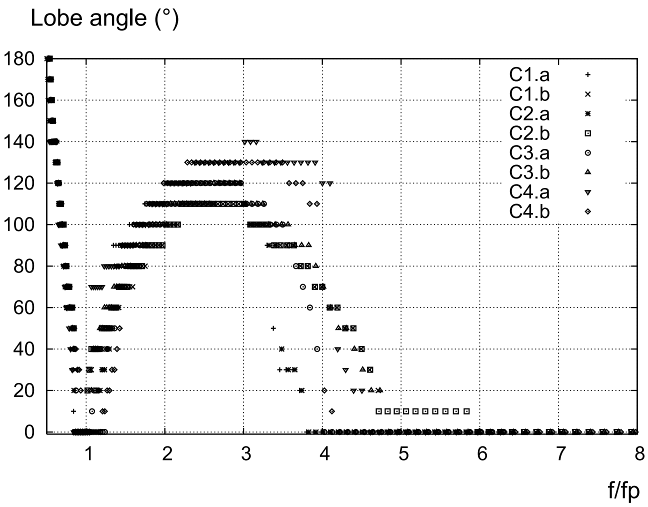

Figure 12. Angle between the lobes of the wave directional distribution, $2\theta_l$, versus f/f_p at t = 128 h for the eight simulated cases using GQM.

GQM is rather similar for the eight cases (not shown), although some differences were noted. In particular, the HF bimodality is more pronounced in case C4, especially in case C4.a, than in the other ones. DIA gives a much more widespread directional distribution at $f > f_p$ and no clear bimodality. The low-frequency (sometimes referred to as LF) bimodality is more pronounced when using an exact method for Q_{nl4}, as already described by *Hisaki* [2007].

4. Influence of Wind Input and Dissipation

4.1. Model Equation and Initial Conditions

[51] In this section, we examine the influence of wind input and dissipation, in addition to wave-wave nonlinear transfers, on the evolution of the wind-wave spectrum. This is typical of a duration-limited wave growth case [e.g., *Young*, 1999]. This case was chosen as a first step in our work for faster simulation times (the "point model" version of our code). Extension to 1-D situations (e.g., fetch-limited cases) is now under consideration and will be reported in a separate paper. A constant wind of 10 m s^{-1} is considered. We test three combinations (sets I, II, and III) of the wind input (Q_{in}) and dissipation (Q_{wc}) terms (see Table 2). Set I corresponds to WAM cycle 3 with the wind parameterization of *Snyder et al.* [1981] and the whitecapping dissipation of *Hasselmann* [1974] as formulated by *Komen et al.* [1984]. Set II consists of the expression of *Yan* [1987] for Q_{in} with the parameter values of *Van der Westhuysen et al.* [2007], combined with the whitecapping model of *Van der Westhuysen et al.* [2007] and *Van der Westhuysen* [2008]. Set III corresponds to WAM cycle 4 with the *Janssen* [1989, 1991] wind input model and the Q_{wc} model of *Komen et al.* [1984] with the coefficient values proposed in WAM cycle 4 [*Günther et al.*, 1992]. Set III is run with two options: no

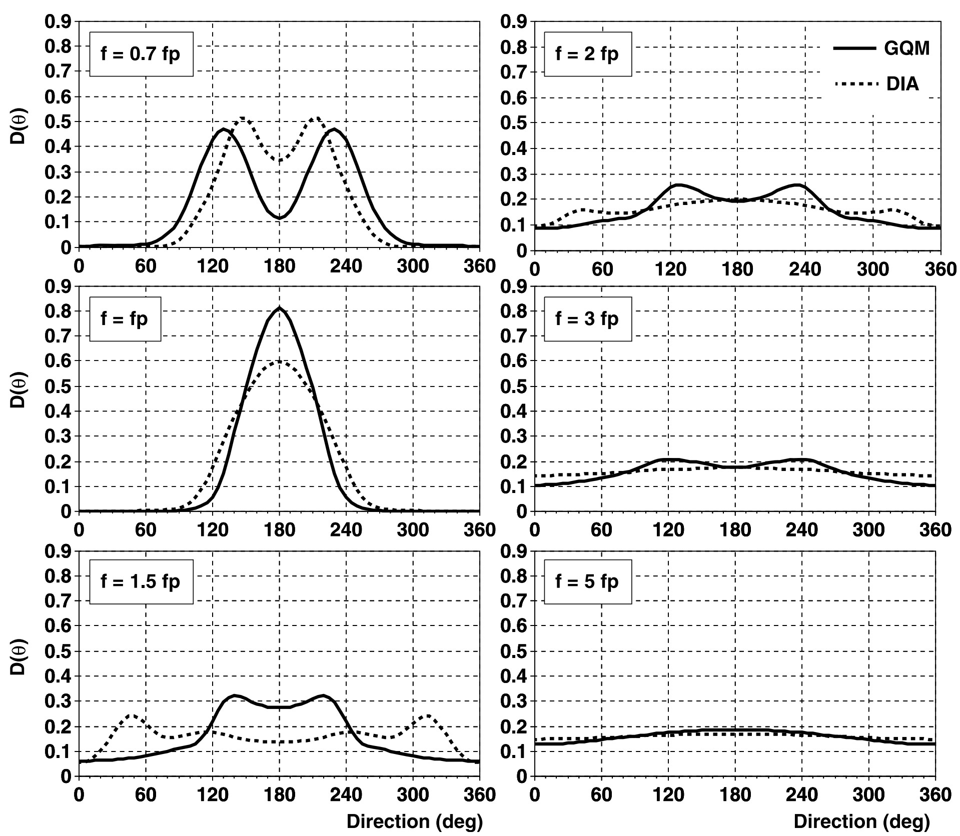

Figure 13. Sections of the directional spreading function $D(f, \theta)$ at t = 128 h, at six frequencies ($f = 0.7f_p$, $f = f_p$, f = 1.5f_p, f = 2f_p, f = 3f_p, and f = 5fp) for case C3.b: GQM (solid lines) and DIA method (dashed lines).

Table 2. Description of the Sets (I, II, III) and Options (free tail or imposed tail)

Set	Q_{in}	Q_{wc}	Tail Option
I (WAM Cycle 3)	*Snyder et al.* [1981]	*Komen et al.* [1984]	free tail
II	*Yan* [1987]	*Van der Westhuysen et al.* [2007]; *Van der Westhuysen* [2008]	free tail
III-ft	*Janssen* [1989, 1991]	*Komen et al.* [1984]; *Günther et al.* [1992]	free tail
III-it (WAM Cycle 4)	*Janssen* [1989, 1991]	*Komen et al.* [1984]; *Günther et al.* [1992]	imposed f^{-4} tail

parametric tail [free tail (ft)] or f^{-4} HF tail imposed over the frequency range $[f_d, f_{max}]$ [imposed tail (it)] as implemented in WAM cycle 4. It should be noted that, among the parameterizations used here, sets I and III-it are the only ones that were tested in a wide range of sea states.

[52] We chose to use some traditional parameterizations (sets I and III) and a more recent one for the dissipation (set II). This is, of course, a restricted choice but it allows some interesting differences in the evolution of the spectrum to be highlighted. Moreover, we may note that some questions have been raised about the validity of set II at large scales [*Ardhuin and Boyer*, 2006]. For completeness, the reader should refer, for instance, to the recent work of *Babanin et al.* [2007a, 2007b] and *Ardhuin et al.* [2008, 2009]. The parameterizations of *Tolman and Chalikov* [1996] or *Bidlot et al.* [2005] could also be interesting candidates.

[53] As previously, all the simulations were run using the GQM and DIA method for comparison. The parameters of the source and sink terms were not retuned when the method for calculating the Q_{nl4} term was changed. For instance, the model of *Van der Westhuysen et al.* [2007] for Q_{wc} was computed with the coefficients C_{ds} = 5.0 10^{-5} and B_r = 1.75 10^{-3}, calibrated for DIA simulations.

[54] Simulations were run from the initial cases C*i*.a described in section 3. Because the evolution of the spectrum is strongly influenced by the amount of energy brought by the wind, we estimated that it was not useful to test two different values of $H_{m0,init}$.

[55] In the simulations the discrete frequency-direction grid is composed of 128 frequencies, with geometric spacing (f_{i+1}/f_i = 1.031) from $f_{p0}/25$ (0.04 Hz) to $2f_{p0}$ (2 Hz) and 72 directions with a constant spacing of 5°. The simulations were run during 96 h of physical time.

4.2. Evolution of Representative Sea State Parameters

[56] Time evolutions of H_{m0}, T_p, and σ are plotted in Figure 14 for set II. The values of H_{m0} and T_p are increasing and become quasi-steady after 48 h of simulation when using GQM, and close to the end of the simulation for DIA. At first sight, there is almost no difference between the curves obtained from the four initial cases C*i*.a. Plots in a logarithmic scale show few differences at the initial stage (first few minutes) for H_{m0} and T_p. These differences are more pronounced for σ, owing to differences in the initial value of σ. However, after about 10 min, the simulations converge to the same value. Figure 14 enables a comparison of DIA and GQM. We recall that the parameters in Q_{in} and Q_{wc} are the same for both simulations and that they were calibrated for DIA simulations. This results in differences between H_{m0} and T_p growth curves. DIA curves are higher for both H_{m0} and T_p, but recalibration of some coefficients could lead to similar results when using GQM. Nevertheless, we emphasize that, under unsteady and turning wind conditions, differences can be much more important [e.g., *Benoit*, 2006]. Unsteady cases are more sensitive to the choice of the method for Q_{nl4}, and DIA was shown to react more slowly to changing conditions. Besides this, DIA gives a larger directional spreading, which is a classical problem of the DIA method.

[57] Figure 15 shows the differences arising from the use of the four sets. Because initial conditions have almost no influence, we choose to consider only C3.a results. At first, significant trends can be noticed: results obtained with set III without parametric tail give much higher H_{m0} and T_p values. They stabilize more slowly and do not really reach the quasi-steady state before the end of the simulation. We analyze precisely the reasons for this very important growth in section 4.3. The three other curves (sets I, II, and III-it) are closer to each other, but still have some differences. The growth curves for H_{m0} and T_p obtained using DIA are slightly higher than those obtained using GQM. Differences are very small when using sets I and III - ft. Although the objective of this work is not to calibrate or validate the parameterizations, it should be noticed that the final values of H_{m0} and T_p for sets I, II, and III-it are quite underestimated compared to the fully developed Pierson-Moskowitz asymptotic limits as reanalyzed by *Alves et al.* [2003], showing some deficiencies of the presently used source terms or a need to calibrate them.

[58] For the mean directional width σ, DIA once again gives a larger directional spreading for whichever parameterization is used to model the source terms. Set I gives a much larger directional spreading than the other sets whenever DIA or GQM is used for Q_{nl4}. This is related to the directional structure and magnitude of the sum Q_{in} + Q_{wc}. For instance, the Q_{in} model has a cosθ directional dependence for sets I and II and a narrower distribution in $\cos^2 \theta$ for set III; therefore, Q_{in} plays a role in the spreading of the angular spectrum, but the relative magnitude and structure of Q_{in} and Q_{wc} are also determinant. The influence of Q_{in} and Q_{wc} on the directional structure of the spectrum is analyzed in section 4.4.

4.3. Evolution of the Frequency Spectrum

[59] Figure 16 reports the evolution of the frequency spectrum $E(f)$ (initial condition C1.a) using sets I–III. For all sets, the evolution of $E(f)$ shows similar trends. It evolves rapidly during the first few minutes. The spectral peak appears after about 5 min, then it begins to migrate toward low frequencies, gaining energy from wind input. Then the increase slows down and $E(f)$ stabilizes. It is noted that the three other initial conditions produce the same spectra after a few minutes (figures not reported here).

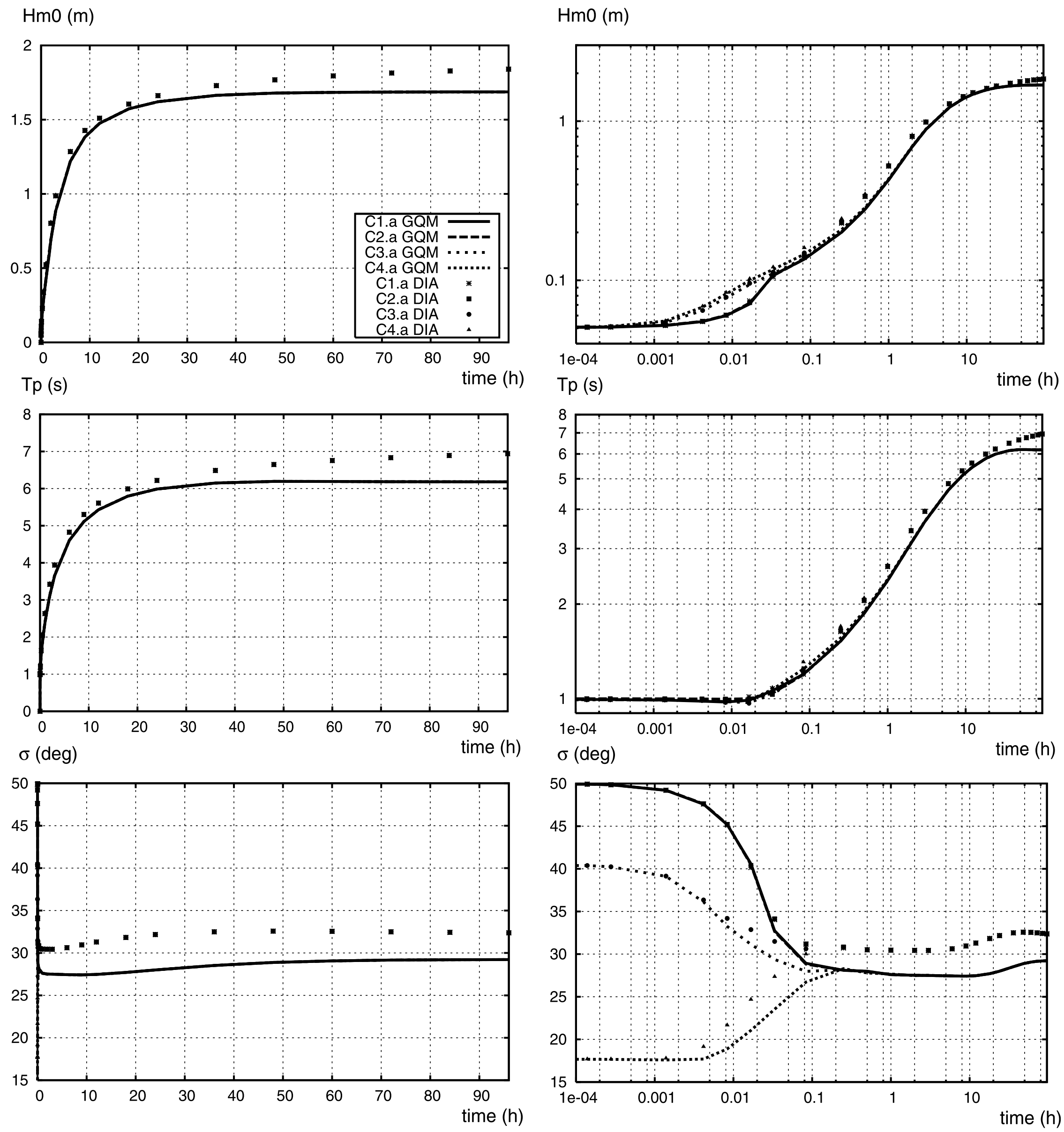

Figure 14. Time evolution of the wave height H_{m0}, the peak period T_p, and the mean angular width σ for the four initial cases. Set II, GQM and DIA method: (left column) linear scale, (right column) logarithmic scale.

[60] The final shape (at t = 96 h) is a little different from the purely nonlinear shape obtained in section 3. It is less peaked and the HF f^{-4} tail is not observed in every case. For example, the f^{-4} HF tail can be only observed over a very limited range for set III-ft (without a constrained tail). At higher frequencies, $E(f)$ decreases much more steeply than observed spectra [*Banner et al.*, 1989; *Young and Babanin*, 2006; *Long and Resio*, 2007] because of dissipation. Differences between DIA and GQM spectra are observed for all the source terms used. At the beginning of the simulation, DIA produces a succession of peaks around the initial step instead of the smooth and regular shape obtained with GQM. The final shape of the DIA spectrum is more spread in frequency.

[61] One can notice that the evolution of the spectra is influenced by the parameterizations chosen for the source and sink terms. Set III-ft gives spectra that have a much higher maximum value and a smaller peak frequency. Moreover, the evolution of the spectrum is not totally stabilized at the end of the simulation. Similar observations were made in section 4.2 for H_{m0} and T_p.

4.3.1. HF Tail: Influence of the Models and of the Constrained Tail

[62] In every studied case, the spectrum is assumed to have an f^{-4} shape above the last discrete frequency. As observed by *Banner and Young* [1994] and verified in our calculations, this only influences the last upper frequencies.

[63] In contrast, applying a constrained tail over $[f_d; f_{\max}]$ can influence the results over the entire frequency domain. In the simulations, at the end of the run (t = 96 h), the diagnostic tail is imposed from $f_d = 3.3 f_p$ when using GQM, and from $f_d = 3 f_p$ with DIA.

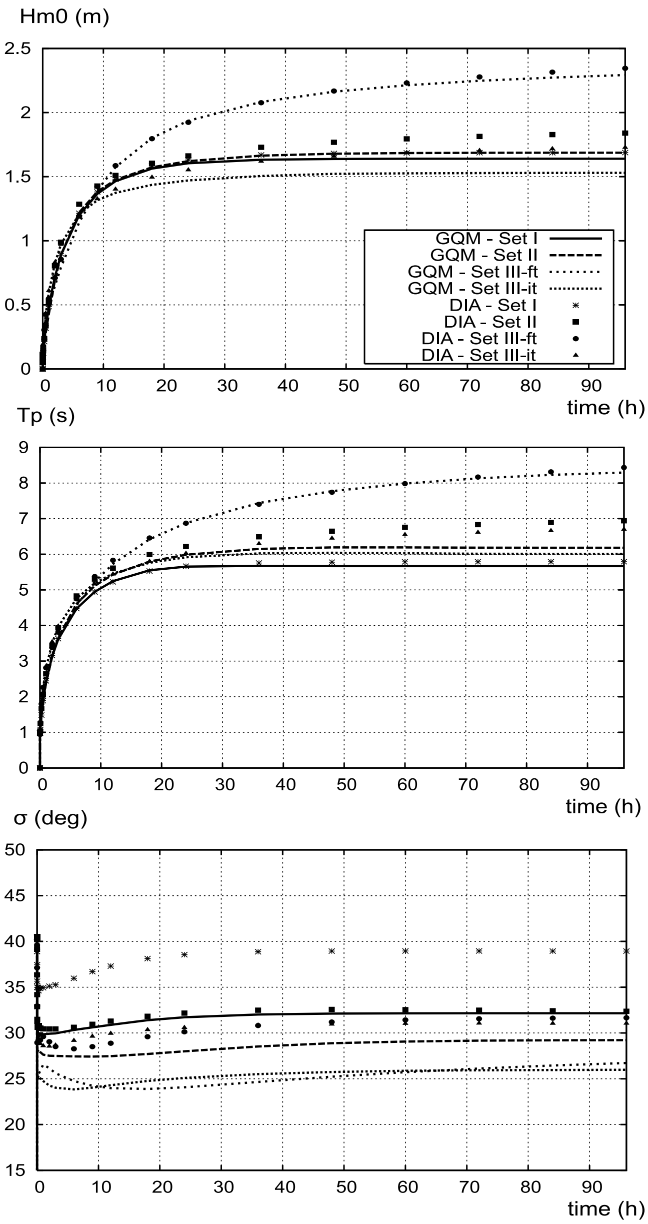

Figure 15. Time evolution of the wave height H_{m0}, the peak period T_p, and the mean angular width σ for initial case C3.a, GQM and DIA methods. Comparison of sets I, II, III-ft, and III-it.

[64] For sets I, II, and III-ft, no diagnostic tail is imposed over the frequency domain. Results obtained using sets I and II show a similar evolution, with a HF tail close to f^{-4}: $f^{-3.97}$ and $f^{-3.85}$ for set I with GQM and DIA, respectively, and $f^{-4.18}$ for set II with both DIA and GQM. Note that *Van der Westhuysen et al.* [2007] found an $f^{-4.1}$ decay with forcing terms corresponding to set II when modeling a fetch-limited case. Results from set III-ft show a much steeper HF tail with a slope increasing sharply with frequency and decaying much faster than the *Banner et al.* [1989] f^{-5} equivalent in terms of k spectrum. Such a behavior is not supported by theoretical analyses or by observations. This much steeper tail is caused by the strong dissipation at high frequencies of the implementation in WAM cycle 4 of the *Komen et al.* [1984] model.

[65] Set III-it (imposed f^{-4} tail) gives results that are in better agreement with theory and observations than set III-ft. Adding such a parametric tail is not very physical, it just compensates the deficiencies of the parameterizations of set III (WAM4).

[66] The influence of an imposed HF tail on the computed spectrum was examined by *Banner and Young* [1994], who showed, as we also found, the importance of an accurate modeling of the HF part of the spectrum and the significant influence of a constrained tail on the development of the entire spectrum. However, according to *Komen et al.* [1984] and the *WAMDI Group* [1988], the precise form of the diagnostic tail has no influence on the results.

[67] We also made some tests using set I and a constrained tail f^{-4} to see what happens when the modeled tail is very close to the imposed one. As expected, GQM simulations with or without f^{-4} give nearly the same results.

[68] The main reason why the high-frequency range of the spectrum can significantly affect all its evolution, while such low levels of energy are involved, is related to the influence of the HF part of the spectrum on the terms Q_{in} and Q_{wc}. When the energy is increased at high frequencies, the dissipation of *Komen et al.* [1984] is increased and the wind input of *Janssen* [1991] is reduced, which leads to a slowdown in the growth of the spectrum. Figure 17 shows the impact of imposing an f^{-4} HF tail on the calculated source and transfer terms: it results in an increase of the dissapation over the whole frequency domain and in a decrease of the wind input at the spectral peak. This is attributed to the presence of integrated parameters (like m_0 and the mean frequency) in the Q_{wc} formula and to a pronounced feedback via the friction velocity u* and the wave-induced stress in *Janssen*'s, [1991] Q_{in} formula. Thus, the sum $Q_{\text{in}} + Q_{\text{wc}}$ is strongly reduced around the spectral peak frequency. At the same time, the Q_{nl4} term is not significantly affected near f_p. The sum of the three terms is plotted in the range 0.04–0.5 Hz for more visibility. Observations of the positive and negative peaks show that the total source term was reduced by the imposition of the f^{-4} tail. This therefore explains the artificial increase of wind-wave energy in the absence of a diagnostic tail (III-ft).

[69] *Banner and Young* [1994] proposed an alternative explanation. According to these authors, a smaller level of energy at high frequencies results in an increase of the Q_{nl4} term and thus leads to a larger growth of the spectrum. This explanation was not retained here. As seen in Figure 17, the imposition of a HF f^{-4} tail has a small impact on the global nonlinear energy transfers. The effects on Q_{nl4} at high frequencies are important, as seen in the curve representing the relative nonlinear transfer term $Q_{\text{nl4}}/E(f)$ (Figure 17e), but the impact on the overall evolution of the spectrum is not significant as compared with the pronounced effect of Q_{in} and Q_{wc}.

4.3.2. Analysis of Source Terms Balance in the High-Frequency Range

[70] The slope of the HF tail can be explained by the balance of the source terms. It was shown in section 3 that, without any forcing term, the HF tail is close to $f^{-4.1}$. The quadruplet interactions tend to maintain a shape close to f^{-4} at high frequencies, as shown by *Zakharov and Filonenko*

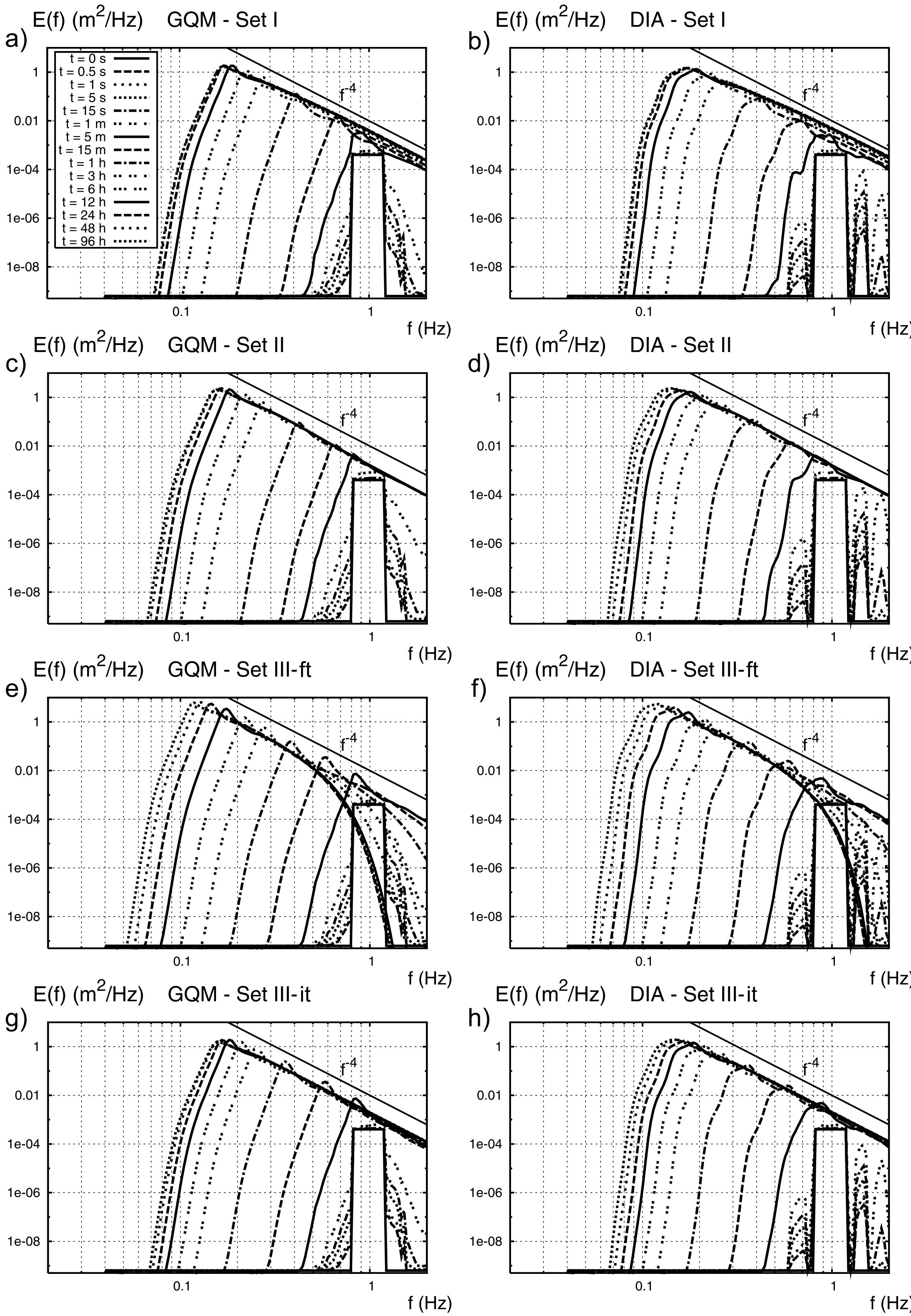

Figure 16. Evolution of the frequency spectrum $E(f)$ (from 0 to 96 h) for the initial case C1.a: GQM with sets (a) I, (c) II, (e) III-ft, and (g) III-it, and DIA method with sets (b) I, (d) II, (f) III-ft, and (h) III-it.

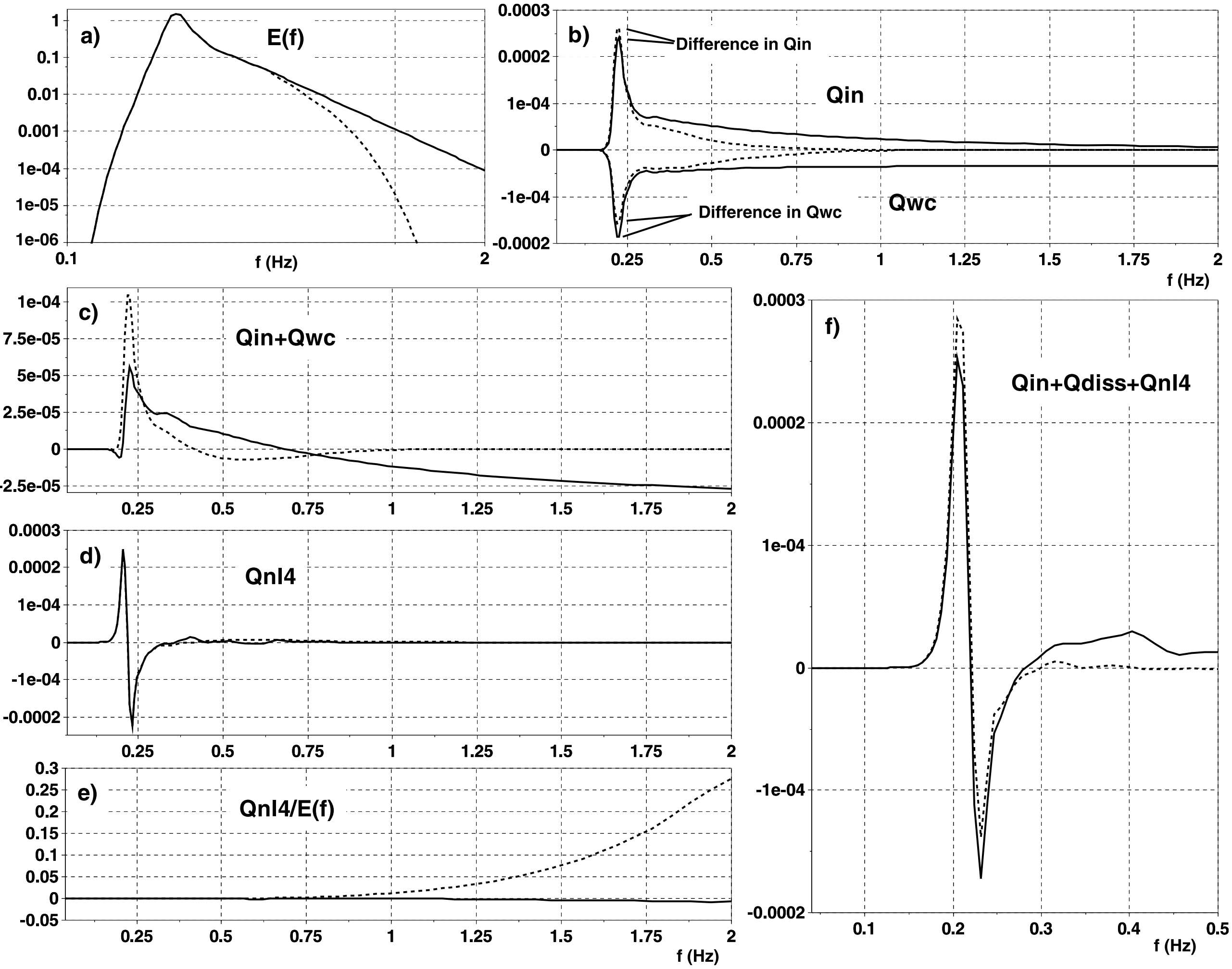

Figure 17. Influence of the HF tail on the evolution of the spectrum. (a) The frequency spectrum $E(f)$ simulated with set III-ft and GQM at t = 6 h is considered (dotted line). An f^{-4} tail is applied to this spectrum (solid line). (b) $Q_{\rm in}$ [*Janssen*, 1989, 1991] and $Q_{\rm wc}$ [*Komen et al.*, 1984; *Günther et al.*, 1992] are calculated from both spectra. (c) $Q_{\rm in}$ + $Q_{\rm wc}$. (d) $Q_{\rm nl4}$ (GQM). (e) Relative nonlinear transfer term $Q_{\rm nl4}/E(f)$. (f) Total source term $Q_{\rm in}$ + $Q_{\rm wc}$ + $Q_{\rm nl4}$.

[1966], *Toba* [1973], *Kahma* [1981], *Kitaigorodskii* [1983], *Phillips* [1985], and *Resio et al.* [2001]. To obtain the same slope when input and dissipation are also present, it is necessary that the dissipation and source terms scale similarly with frequency in the HF range [*Resio et al.*, 2004].

[71] We point out that there is quite a strong experimental support of the f^{-4} HF tail for the frequency spectrum in deepwater conditions. The extensive analyses carried out by *Young and Babanin* [2006] on Lake George data revealed that the mean value of the exponent n of f^{-n} in the frequency range $5f_p < f < 10f_p$ lies close to 4 (3.9 actually). Considering the range of values of f_p of this data set, *Young and Babanin* [2006] noted that the spectral components in this frequency range were always in deepwater conditions.

[72] However, some observations in real sea conditions indicate that an f^{-4} high-frequency shape applies up to few times f_p and then decays is somewhat faster with frequency. For instance, spectra presented by *Long and Resio* [2007] for particular conditions with short fetches and proximity of coastlines in Currituck Sound revealed a decay closer to f^{-5} when f is greater than two or three times f_p.

[73] In the HF range, the wind input terms vary as $f^2\,E(f)$, $f^3\,E(f)$, and $f^3\,E(f)$ for sets I, II, and III, respectively. *Yan* [1987] parameterization (set II) is a combination of the *Janssen* [1991] (set III) and *Snyder et al.* [1981] (set I) terms and scales like Janssen's one in the HF range. The dissipation terms for sets I, II, and III vary as $f^2\,E(f)$, $f^{11}\,E(f)^3$, and $f^4\,E(f)$, respectively. When considering the combined effect of $Q_{\rm in}$ and $Q_{\rm wc}$, one can notice the following:

[74] 1. For set I, $Q_{\rm in}$ and $Q_{\rm wc}$ scale similarly at high frequencies [as $f^2\,E(f)$]. When $E(f) \propto f^{-4}$ in the HF range, they behave like f^{-2}.

[75] 2. For set II, when $E(f) \propto f^{-4}$ in the HF range, $Q_{\rm in}$ and $Q_{\rm wc}$ also scale similarly at high frequencies and both tend to f^{-1}.

[76] 3. For set III, in contrast, $Q_{\rm in}$ and $Q_{\rm wc}$ scale differently. If we again assume that $E(f) \propto f^{-4}$ in the HF range, $Q_{\rm in} \propto f^{-1}$ and $Q_{\rm wc} \propto 1$. This raises questions about the validity of the dissipation term: the f^{-4} or even f^{-5} shape of

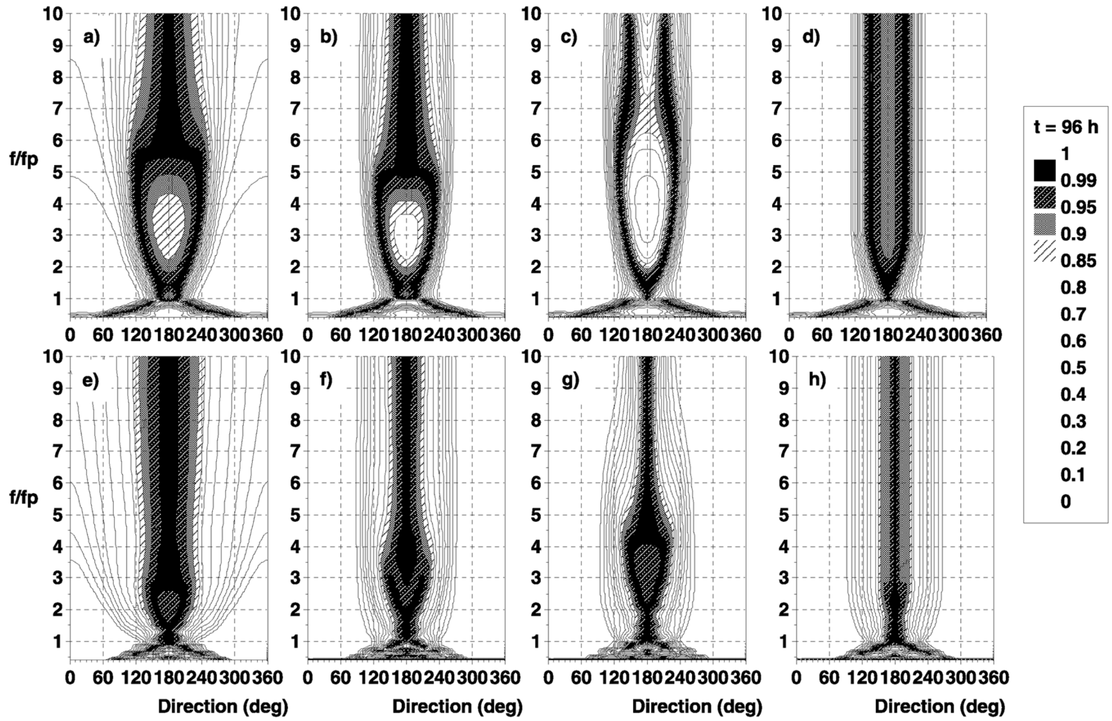

Figure 18. Normalized directional spreading function $\tilde{D}(f/f_p, \theta)$ at t = 96 h for the initial case C2.a: GQM with source terms (a) I, (b) II, (c) III-ft, and (d) III-it; DIA method with source terms (e) I, (f) II, (g) III-ft, and (h) III-it.

the spectrum could not be maintained with this source balance and with such a strong high-frequency dissipation. This is the reason why we observe with set III-ft a very steep HF tail. This in turn could also justify the motivation of using an imposed parametric tail: it can help in improving the prediction of parameters such as H_{m0} and T_p and eventually of the frequency spectrum. However, it also modifies the whole directional structure of the spectrum (see section 4.4).

4.4. Angular Spreading of Wave Energy

[77] Figure 18 reports the normalized directional spreading function $\tilde{D}(f/f_p, \theta)$ at t = 96 h obtained from the initial spectrum C2.a (but results are almost the same for the four cases) using the different source terms.

[78] GQM simulations give here again a bimodal structure of the directional spectra at frequencies lower and higher than f_p. The low-frequency structure of the spectrum is very close to the one observed in section 3. Nonlinear interactions are responsible for the two directional lobes. However, the structure also depends on the parameterizations of the source terms.

[79] As in section 3, the directional distribution has a very marked bimodal structure at $f < f_p$, slim down around the peak frequency, and is bimodal above f_p. A transition to unimodality above $5f_p$ is observed for sets I and II. Set I gives a more spread directional distribution than sets II and III for frequencies above f_p. In all cases, the directional distribution obtained when forcing terms are present is narrower at frequencies above the peak than the one of section 3. This shows the influence of the source and sink terms on the wave directional distribution. In section 3, the calculated mean directional width σ was around 40–50°. When adding wind input and dissipation, σ is reduced to 26–33° for the GQM runs (see also Figure 15).

[80] It is not straightforward to analyze the combined effects of Q_{in}, Q_{wc}, and Q_{nl4} on the directional distribution of the spectrum. The Q_{nl4} term plays a major role in determining the directional spreading of the spectrum [*Young and Van Vledder*, 1993], redistributing energy in directions oblique to the wind, as shown in section 3.5. But whatever the parameterization of the terms Q_{in} and Q_{wc}, the spectrum always evolves to an equilibrium shape [*Banner and Young*, 1994]. This means that Q_{nl4} always acts to balance the sum $Q_{\text{in}} + Q_{\text{wc}}$ [*Young and Van Vledder*, 1993] and shows the importance of the sum $Q_{\text{in}} + Q_{\text{wc}}$, as confirmed by our simulations.

[81] The angular distribution of Q_{in} is determined by the product of $\cos\theta$ (or $\cos^2\theta$) and $F(f, \theta)$, whereas that of Q_{wc} is only determined by $F(f, \theta)$ for the parameterizations chosen here. Therefore, Q_{in} decreases faster than Q_{wc} with θ. From some angle value, the sum $Q_{\text{in}} + Q_{\text{wc}}$ thus becomes negative. Because Q_{nl4} acts to compensate the sum $Q_{\text{in}} + Q_{\text{wc}}$ when the directional stability is achieved, it is clear that this angle influences the directional spreading of the spectrum. A narrower directional distribution of the input term or a stronger dissipation then influences the directional spreading function. For example, the Q_{in} model of set III has a narrow $\cos^2\theta$ distribution. Thus, the sum $Q_{\text{in}} + Q_{\text{wc}}$ starts being negative at angles smaller than for a $\cos\theta$ distribution (sets I and II). This could explain why the directional spreading is smaller with the parameterizations of set III. But the relative magnitudes of Q_{in} and Q_{wc} also have an influence. Keeping the same input term, a stronger dissipation (as for WAM 4, set III) leads to a smaller directional

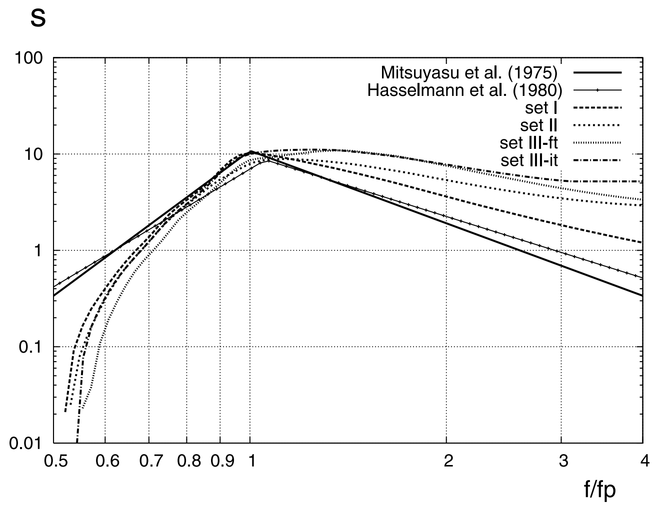

Figure 19. Parameter s of the cardioid model for the directional distribution as a function of f/f_p at $t = 96$ h. GQM, sets I, II, III-ft, and III-it, for initial case C2.a. Comparison with expressions of *Mitsuyasu et al.* [1975] and *Hasselmann et al.* [1980].

spreading. Set I has the smallest dissipation and gives the more widespread distribution.

[82] A slight bimodality at f_p becomes visible after 9 h of simulation for set II and 12 h for set I, whereas the distributions obtained with set III are unimodal from $0.95f_p$ to $1.4f_p$ (see also Figure 21). Bimodality at the peak was also recently obtained from simulations by *Korotkevich et al.* [2008], who used a modified version of the WRT method [*Webb*, 1978; *Resio and Perrie*, 1991] for calculation of the nonlinear interactions and three different models for the Q_{wc} term. Their Figures 27 and 28 show spectra with a strong bimodality at the spectral peak.

[83] For sets III-ft and III-it, results show directional distributions that are not unimodal at $f \geq 5f_p$. When the parametric tail is not imposed (set III-ft), the HF bimodality is more pronounced than for sets I and II. The angle between the lobes, $2\,\theta_l$, increases to a maximum around 100° at $f \approx 4f_p$. Then $2\theta_l$ decreases to a value around 60° and remains constant.

[84] Differences in the structure of $\tilde{D}$ for $f \geq 5f_p$ (unimodality or bimodality) are related to the source terms balance. The unimodality of the directional distribution at these high frequencies is associated with low values of Q_{nl4}. For set III-ft, the input and dissipation terms do not scale similarly with frequency at high frequencies (see section 4.3.2). Thus, the Q_{nl4} term has to compensate for the difference between Q_{in} and Q_{wc}, and it does not take low values in comparison with $F(f, \theta)$, as seen in Figure 17e: the relative term $Q_{nl4}/E(f)$ is much more important at high frequencies when the HF tail is steeper. This explains the process that maintains bimodality at higher frequencies in case III-ft. For sets I and II, the proper balance of the source and sink terms at high frequencies leads to smaller values of Q_{nl4} in comparison with $F(f, \theta)$. As in section 3, we thus observe a transition to unimodality for $f \geq 5$–$6f_p$. This simulation result needs to be validated against sufficiently accurate measurements and analyses at these high frequencies.

[85] Regarding the results of set III-it, for frequencies above f_d (here $f_d \approx 3.3f_p$), the directional distribution is forced to be equal to the one obtained at $f = f_d$. Thus, the directional distribution cannot be consistent with observations, at least at frequencies $f > f_d$. Furthermore, the bimodality above f_p is less pronounced. Thus, we see that the HF tail has an influence, not only on the energy level and spectral peak (section 4.2) and on the high-frequency shape (section 4.3) but also on the overall directional distribution.

[86] Figures 18e–18h show the same simulations carried out using DIA. The directional distributions are narrow near the spectral peak. The spectra obtained with sets I, II, and III-ft show some broadening at $f > f_p$, and a very slight bimodality can even be noticed. As for GQM simulations, set I produces a more spread spectrum. The distribution obtained using set III-it does not show any HF bimodality. In all cases, at low frequencies, some bimodality exists but the results are quite noisy compared to GQM results. Comparison of these results with the DIA distribution obtained in section 3 shows several differences. The DIA distribution without any forcing term is much more spread and noisy for frequencies above f_p. The directional distributions of sections 3 and 4 are quite similar at low frequencies.

[87] Similar simulations of the homogeneous KE were recently performed by *Hisaki* [2007] using the WAM cycle 3 parameterizations of Q_{in} and Q_{wc} and two methods to calculate Q_{nl4}: DIA and an other exact method called RIAM [*Komatsu and Masuda*, 1996]. Directional distributions are also bimodal below f_p. The distribution calculated with the exact method shows high-frequency bimodality.

4.5. Comparison with Measured Wave Directional Distributions

4.5.1. Comparison with the Expressions of *Mitsuyasu et al.* [1975] and *Hasselmann et al.* [1980]

[88] The structure of $D(f, \theta)$ obtained from GQM simulations at the final simulation time ($t = 96$ h) is compared to the widely used parametric expressions of the form $\cos^{2s}[(\theta - \theta_0)/2]$ (cardioid model), where s is a parameter that was determined by the pioneering works of *Mitsuyasu et al.* [1975] and *Hasselmann et al.* [1980]. These parameterizations were proposed on the basis of temporal measurements recorded by directional buoys. Results show that most of the energy is propagating in the wind direction, that it decays with increasing angle to the wind direction, and that the directional spreading is narrowest near the spectral peak and broadens toward both higher and lower frequencies. Note that the models of *Mitsuyasu et al.* [1975] and *Hasselmann et al.* [1980] were designed in the f/f_p intervals 0.3–3 and 0.3–4, respectively. If one assumes that D can be fitted to the given parametrical unimodal expression $A \cos^{2s}[(\theta - \theta_0)/2]$, we can calculate the corresponding parameter s using the method of *Longuet-Higgins et al.* [1963]. In our case, $\theta_0 = 180°$. The parameter s is given in Figure 19 for the directional distributions obtained with sets I, II, and III. The curves of *Mitsuyasu et al.* [1975] and *Hasselmann et al.* [1980] are superimposed (the value $U_{10}/C_p = 1.03$ is taken, corresponding to set II). Results show the narrowing of the directional distribution near the spectral peak (s is a maximum around 1 to $1.3f/f_p$, depending on the source terms) and

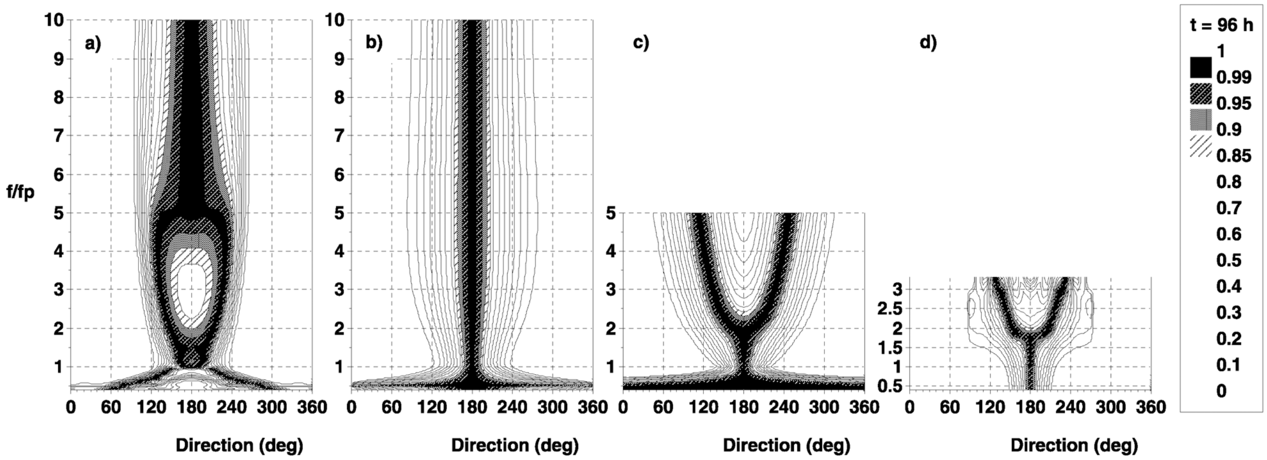

Figure 20. Normalized directional spreading function $\tilde{D}(f/f_p, \theta)$ at t = 96 h: (a) GQM, source terms II, for initial case C2.a. (b) $A\cos^{2s}[(\theta - \theta_0)/2)]$. (c) *Ewans*' [1998] model. (d) fast Fourier transform with nine terms *Hwang et al.* [2000b].

the increase of the directional spreading toward low and high frequencies. For frequencies greater than $1 - 1.3f_p$, s decreases quite slowly and then stabilizes for sets II and III, while the results of *Mitsuyasu et al.* [1975] or *Hasselmann et al.* [1980] do not suggest such a tendency toward stabilization. Note that the s value of set III-it (with constrained tail) is constant after $f = f_d$. The parameter s obtained with set I does not stop decreasing, but with a smaller slope than the curves of *Mitsuyasu et al.* [1975] and *Hasselmann et al.* [1980]. We conclude that the $\cos^{2s}[(\theta - \theta_0)/2]$ relationship allows some major features of the directional distribution to be represented but gives a very incomplete representation of $\tilde{D}$ (Figure 20b).

4.5.2. Comparison with Bimodal Distributions: Measurements and Parameterizations

[89] Bimodal directional distributions had been observed since the 1990s from buoy or wave gauge data, but large uncertainties remained. Since the 2000s, thanks to new means of measurements [e.g., *Hwang et al.*, 2000a, 2000b], the accuracy of the data was increased and new evidence showed that the structure of the directional spectrum can be bimodal. Bimodal parametric relationships were suggested by *Ewans* [1998] and *Hwang et al.* [2000b]. *Ewans* [1998] proposed a double Gaussian parameterization, and *Hwang et al.* [2000b] presented a Fourier decomposition of their measured directional distribution. These parametric relationships both show the bimodality of the directional spectrum at frequencies above f_p and are unimodal below f_p. The LF bimodality was observed by *Wang and Hwang* [2001] and by *Hwang et al.* [2000b], who proposed parameterizations of the lobe angle that are bimodal at low frequencies. *Ewans* [1998] also noticed bimodal distributions at $f < f_p$.

[90] Figure 20c shows the results from the work of *Ewans* [1998]. There is an interesting agreement with our results at high frequencies but some differences can be observed. The angle between the lobes is zero below $f = 2.4f_p$ and then grows without stabilizing, while θ_l obtained using GQM starts growing around 0.95 to $1.4f_p$, depending on the models employed, and then stabilizes or again becomes equal to zero. We emphasize that the parameterization of *Ewans* [1998] was designed on the basis of heave-pitch-roll buoy measurements, delivering a limited number of independent parameters to estimate the angular distribution at each frequency and whose precision might be questionable for high frequencies.

[91] Our results are also quite close to the Fourier decomposition of *Hwang et al.* [2000b] (Figure 20d) for 1.8 $\leq f_p \leq 3.3$. The value of θ_l given by *Hwang et al.* [2000b] is zero up to $f = 1.8f_p$.

[92] The lobe ratio, noted r_{lobe}, is defined as the ratio of the maximum value of $D(f, \theta)$ to its value at the dominant wave direction (θ_0 = 180°). Figure 21 compares our modeling results for θ_l and r_{lobe} with the experimental results of *Ewans* [1998] and *Hwang et al.* [2000a, 2000b]. We restrict our comparisons to $0.6 \leq f/f_p \leq 3.3$. The measurements of *Hwang et al.* [2000a, 2000b] correspond to a spatially homogeneous and quasi-steady wave field with a mean wind speed of 9.5 m s^{-1} and an inverse wave age $U_{10}/C_p \approx$ 0.98. The inverse wave age for sets I, II, and III-it at t = 96 h ($U_{10}/C_p \approx$ 1.1, 1.03, and 1.06, respectively) is slightly larger than the one given by measurements. For set III-ft, U_{10}/C_p is much smaller (≈0.77).

[93] All the models, simulations, and measurements give lobe angles that agree well above $f/f_p = 2$ except for set III-it, which gives a slightly lower angle. The transition to bimodality at $f > f_p$ depends on the models used for Q_{in} and Q_{wc}, which is consistent with the simulation results of *Alves and Banner* [2003]. Results from set III-ft are the closest to the data of *Hwang et al.* [2000a, 2000b]. Sets I and II show a slight bimodality around the peak, which is not in agreement with the results of *Hwang et al.* [2000b] or *Ewans* [1998]. For $f \leq f_p$, the measured θ_l is two to three times smaller than our calculated angles, but in both cases the existence of the LF bimodality is clear. The Fourier decomposition of *Hwang et al.* [2000b] and the parameterization of *Ewans* [1998] are also very close to our results above $1.8f_p$ and $1.9f_p$, respectively, but are unimodal below.

[94] Our results underestimate r_{lobe} at $f > f_p$ compared to the measurements of *Hwang et al.* [2000a, 2000b], which

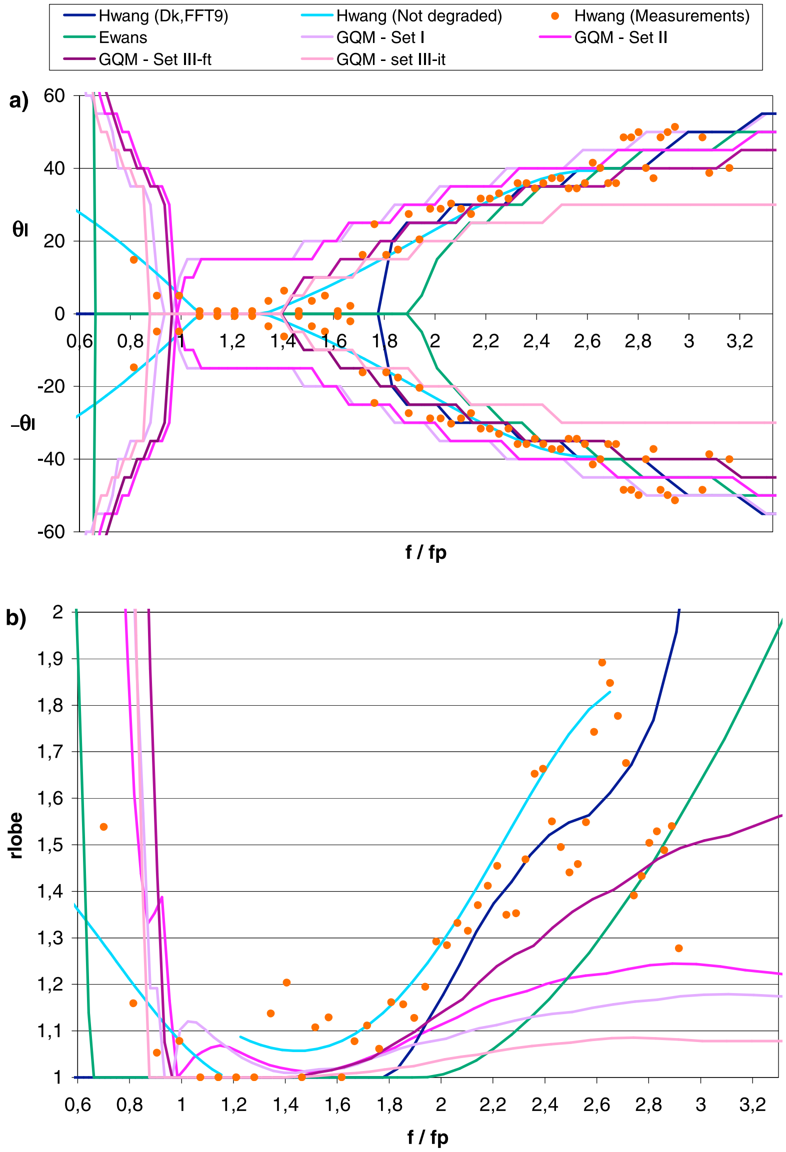

Figure 21. (a) Angle between the lobes and the main direction $-\theta_l$, θ_l; (b) lobe ratio r_{lobe} versus f/f_p at t = 96 h, for the initial case C2.a, GQM, source terms I, II, III-ft, and III-it. Comparison with data of *Hwang et al.* [2000a, 2000b] (measurements with an airborne scanning lidar system, Fourier decomposition with nine components $D_{k,\mathrm{FFT9}}$, and polynomial fitting not degraded; see Figure 10 and Table 2 of their paper) and the *Ewans* [1998] parameterization.

means that the high-frequency bimodality is more pronounced than it appears in our simulations. *Ewans* [1998] gave a lobe ratio smaller than ours up to 2.3–2.8f_p, but it then increases rapidly. Set III-ft gives higher r_{lobe} values than the other sets, which is related to the balance of the source and sink terms and the strong high-frequency dissipation (see section 4.4). Set III-it gives the smallest r_{lobe} values. At $f < f_p$, our simulations give a higher r_{lobe}, but measurements also show bimodality.

[95] The lobe ratio is also calculated from GQM simulations of section 3 (purely nonlinear case) for comparison. The value of r_{lobe} is again globally smaller than observations at $f > f_p$ (figure not reported here). It increases to a maximum value of 1.33 at $f = 2.2f_p$ (quite close to observations) and then decreases. This suggests the influence of wind input and dissipation on the r_{lobe} magnitude at $f > f_p$.

[96] *Alves and Banner* [2003] compared simulations using several parameterizations of Q_{in} and Q_{wc} to the data of *Hwang et al.* [2000b] for a constant inverse wave age $U_{10}/C_p = 0.98$. They found a lobe angle close to that of *Hwang et al.* [2000b] at $f > 2f_p$ and a generally smaller lobe ratio. Their results point out the influence of Q_{in} and Q_{wc} on r_{lobe} values.

[97] We observed that higher values of r_{lobe} were obtained at earlier times, suggesting a dependence on wave age (Figure 22). Our analysis indicates that the highest lobe ratios are most of the time observed when the nonlinear transfers are a maximum and the redistribution of energy to oblique angles is the largest. Curves representing sets II, III-ft, and III-it have a bell shape. The value of r_{lobe} increases

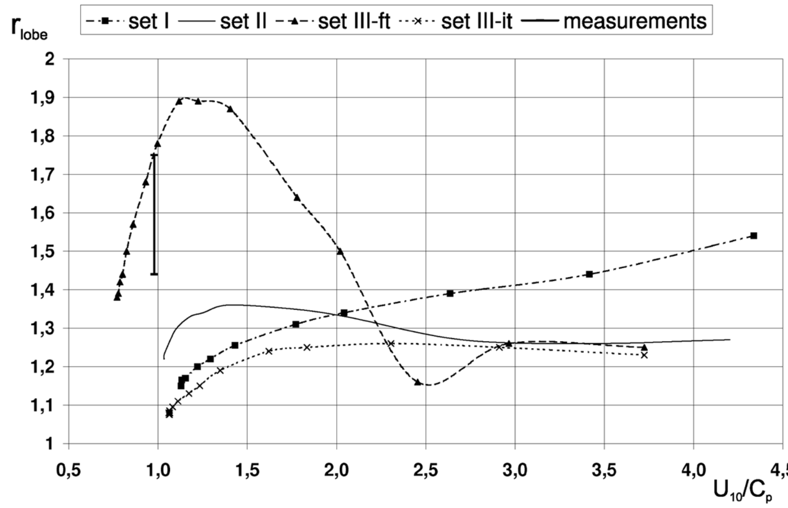

Figure 22. Lobe ratio r_{lobe} versus inverse wave age U_{10}/C_p for $f = 2.5f_p$: initial case C2.a, GQM, and source terms I, II, III-ft, and III-it.

with the inverse wave age up to a maximum value and then decreases. The set III curve increases with U_{10}/C_p. Measurements by *Hwang et al.* [2000b] at $f = 2.5f_p$ are given with an error bar and seem closer to results of set III-ft. Our results also indicate a small dependence of the lobe angle on U_{10}/C_p, in agreement with the observations of *Ewans* [1998] and *Long and Resio* [2007]. This analysis might deserve additional studies or investigations.

4.6. Discussion About the Low-Frequency Bimodality

[98] Our simulations showed that a fundamental feature of the spectrum is the low-frequency bimodality, which is present whenever using GQM or DIA, with or without forcing terms. *Young et al.* [1995] also observed LF bimodality on their simulated spectra, but they argued that a "strong bimodal spreading for $f/f_p < 1$" was "in contrast to the measured results which are broad and unimodal in this region" and discussed possible causes of this feature. This raises the question whether the LF bimodality comes from the numerical models or is a real feature of ocean waves. According to *Young et al.* [1995], there is always a small atmospheric input at frequencies below f_p, which is enough to dominate the nonlinear term and make the directional distribution unimodal. They stated that, because there is no atmospheric input in the models at frequencies below the peak, the directional distribution is only controlled by nonlinear terms and becomes bimodal.

[99] In our simulations, there is a small but positive input at frequencies lower than the peak. The initial spectrum is nonzero over the whole frequency domain. Therefore, the atmospheric input is equal to zero only if the growth rate β (defined as $\beta(f, \theta) = Q_{\mathrm{in}}(f, \theta)/[\sigma F(f, \theta)]$) is equal to zero.

[100] For each of the parameterizations used here, there is a cutoff frequency below which $Q_{\mathrm{in}} = 0$. This cutoff frequency is smaller than the peak frequency for all the sets when GQM is used, even at the end of the simulation where the peak frequency is small. For the model of *Snyder et al.* [1981] (set I), the cutoff frequency is $f \approx 0.15$ Hz in our simulations, which corresponds approximately to $U_{10}/C = 1$, where C is the wave phase velocity. Below this limit, there is not input from the wind because waves move faster than the wind. The Q_{in} model of *Yan* [1987] with the coefficients given by *Van der Westhuysen et al.* [2007] can take negative values for waves going faster than wind. In set II, we chose to cut the value of β to $\beta = 0$ to avoid negative growth. The cutoff frequency is then again close to 0.15 Hz. The *Janssen* [1991] input term (set III) also has a cutoff frequency, which depends on several parameters, and takes values between 0.095 and 0.11 Hz in the two options (1 and 2) considered here. Thus, in our simulations, the small input does not modify the structure of the LF directional distribution, which is still controlled by the nonlinear term. It seems that a small low-frequency input does not stop the nonlinear term from creating bimodal lobes.

[101] It is very difficult to obtain precise measurements of directional spectra at frequencies with low levels of energy. This is the case at low frequencies, where observations are showing the broadening of the spectrum. The interpretation of such a broadening in term of spectral isotropization is questionable. Furthermore, some high-resolution field measurement campaigns, such as the one of *Hwang et al.* [2000a, 2000b], and the buoy data of *Wang and Hwang* [2001] clearly show LF bimodality. Inspection of Figure 7 from the work of *Wang and Hwang* [2001], in particular Figures 7d, 7e, 7i, and 7j, which correspond to energetic sea states (H_{m0} between 3 and 5.2 m), reveal directional spectra with a LF bimodality consistent with our simulations, at least qualitatively. Observations by *Ewans* [1998] also reported bimodality at frequencies lower than f_p, although he suggested that it could eventually come from a swell component in some of the spectra.

[102] All this information makes us think that the low-frequency bimodality is a real feature of natural sea states and is not associated with a limitation of the numerical models.

5. Conclusions and Perspectives

[103] In this study, we investigated the properties of the directional wave spectrum as derived using a quasi-exact

computation (GQM method [*Lavrenov*, 2001]) of nonlinear wave-wave interactions. Two methods for computing the Q_{nl4} term and different expressions for Q_{in} and Q_{wc} were considered. Purely nonlinear and duration-limited cases were both simulated. This enabled us to point out the importance of nonlinear wave-wave interactions and of the accuracy of their computing. The influence of the input and dissipation terms on the results was discussed.

[104] The purely nonlinear case gives us the opportunity to check some theoretical results on the evolution of the significant wave height H_{m0} and the peak period T_p and on the self-similarity of the spectrum [e.g., *Badulin et al.*, 2005]. The GQM algorithm reproduces the theoretical evolutions quite well. The influence of the initial directional spectrum is studied in detail. In the purely nonlinear case, the choice of the initial wave spectrum has a moderate influence on the evolution and final values of H_{m0}, T_p, and the mean angular width σ. However, the shape of the spectrum no longer depends on the initial condition after some minutes. When wind input and dissipation are included in the wave model, the effect of the initial spectrum is very small and almost no difference is seen after a few minutes of simulation.

[105] Analysis of the directional distribution shows that bimodality is a robust feature of the wave spectrum, except near the spectral peak and at frequencies greater than $\approx$4–5f_p, where unimodality may apply. The angle between the two symmetric lobes varies with frequency. Whichever parameterization is used for the wind input and the dissipation terms, the global structure of the spectrum is close to the one observed without any source or sink term up to 4f_p. This demonstrates that nonlinear interactions constitute the key mechanism responsible for bimodality. However, we established that the parameterizations of Q_{in} and Q_{wc} have a quantitative effect on the directional distribution of the spectrum. They can enhance or reduce the magnitude of the bimodal lobes, and they play a role in maintaining bimodality at frequencies greater than 5f_p. The transition to bimodality at frequencies higher than f_p also depends on the parameterizations of Q_{in} and Q_{wc}. Our GQM simulation results are globally consistent with the measurements of *Hwang et al.* [2000a, 2000b], even if we found a smaller lobe ratio at frequencies $f > f_p$ and a more pronounced low-frequency bimodality.

[106] The DIA method, when compared to GQM, gives acceptable results concerning the evaluation of H_{m0} and T_p, but it does not give a good prediction of the directional distribution of the spectrum, particularly at frequencies above f_p.

[107] The influence of the parameterizations of Q_{in} and Q_{wc} on the high-frequency shape of $E(f)$ is highlighted. When Q_{in} and Q_{wc} scale similarly at high frequencies, we obtain a fairly good prediction of the HF tail of the spectrum. When the dissipation is too strong at high frequencies, the frequency spectrum has a very steep HF tail that is not in agreement with theoretical and experimental results. The inclusion of a constrained tail is then required to obtain coherent results. The effects of imposing a parametric tail are significant, not only for the high-frequency part of the spectrum but also for the energy level and peak period and for the global directional distribution. The influence of the HF tail on the whole spectrum is explained by the pronounced effects on the input and dissipation terms near the spectral peak frequency and is essentially caused by the presence of integrated in the Q_{wc} formula.

[108] Investigations are in progress for the simulation of the heterogeneous KE (i.e., including propagation in space of the directional spectrum) with an accurate evaluation of nonlinear four-wave interactions. More "realistic" cases (fetch-limited growth, slanting fetch, combination of swell and wind-sea) are already being simulated using the GQM. Despite a need to further optimize the CPU time (about 80–100 times the CPU time of DIA), results obtained using the GQM method are really encouraging and we plan to implement the method in operational sea wave models, such as TOMAWAC [*Benoit et al.*, 1996]. Extension of the GQM to finite depth is not straightforward but should be worked out, as it has been done for other exact methods [e.g., *Hashimoto et al.*, 1998; *Van Vledder*, 2006].

[109] **Acknowledgments.** We acknowledge Paul Hwang for providing us with 2-D spectrum data measured by an airborne scanning lidar system and for his helpful advice.

References

Alves, J.-H. G. M., and M. L. Banner (2003), Performance of a saturation-based dissipation-rate source term in modeling the fetch-limited evolution of wind waves, *J. Phys. Oceanogr.*, *33*, 1274–1298.

Alves, J.-H. G. M., M. L. Banner, and I. R. Young (2003), Revisiting the Pierson-Moskowitz asymptotic limits for fully developed wind waves, *J. Phys. Oceanogr.*, *33*, 1301–1323.

Andrews, D. G., and M. E. McIntyre (1978), On wave action and its relatives, *J. Fluid Mech.*, *89*, 647–664; corrigendum, 95, 796.

Ardhuin, F., and A. L. Boyer (2006), Numerical modelling of sea states: Validation of spectral shapes, *Navigation*, *54*(216), 55–71.

Ardhuin, F., T. H. C. Herbers, G. P. Van Vledder, K. P. Watts, R. Jensen, and H. C. Graber (2007), Swell and slanting-fetch effects on wind wave growth, *J. Phys. Oceanogr.*, *37*, 908–931.

Ardhuin, F., F. Collard, B. Chapron, P. Queffeulou, J.-F. Filipot, and M. Hamon (2008), Spectral wave dissipation based on observations: A global validation, in *Proceedings of the Chinese-German Joint Symposium on Hydraulics and Ocean Engineering*, pp. 391–400, Darmstadt, Germany.

Ardhuin, F., B. Chapron, and F. Collard (2009), Observation of swell dissipation across oceans, *Geophys. Res. Lett.*, *36*, L06607, doi:10.1029/2008GL037030.

Babanin, A. V., D. Chalikov, I. Young, and I. Savelyev (2007a), Predicting the breaking onset of surface water waves, *Geophys. Res. Lett.*, *34*, L07605, doi:10.1029/2006GL029135.

Babanin, A. V., M. Banner, I. Young, and M. Donelan (2007b), Wave-follower field measurements of the wind-input spectral function. Part III: Parameterization of the wind input enhancement due to wave breaking, *J. Phys. Oceanogr.*, *37*, 2764–2775.

Badulin, S. I., A. N. Pushkarev, D. Resio, and V. E. Zakharov (2005), Self-similarity of wind-driven seas, *Nonlinear Proc. Geophys.*, *12*, 891–946.

Banner, M. L., and I. R. Young (1994), Modeling spectral dissipation in the evolution of wind waves. Part I: Assessment of existing model performance, *J. Phys. Oceanogr.*, *24*, 1550–1570.

Banner, M. L., I. S. F. Jones, and J. C. Trinder (1989), Wavenumber spectra of short gravity waves, *J. Fluid Mech.*, *198*, 321–344.

Benoit, M. (2005), Evaluation of methods to compute the non-linear quadruplet interactions for deep-water wave spectra, paper 52 presented at *5th International Symposium on Ocean Wave Measurement and Analysis (WAVES 2005), Madrid*, Am. Soc. Civil Eng., Reston, Va.

Benoit, M. (2006), Implementation and test of improved methods for evaluation of nonlinear quadruplet interactions in a third generation wave model, paper presented at *30th International Conference on Coastal Engineering*, pp. 526–538, San Diego, Calif., Am. Soc. Civil Eng., Reston, Va.

Benoit, M., and E. Gagnaire-Renou (2007), Interactions vague-vague non-linéaires et spectre d'équilibre pour les vagues de gravité en grande profondeur d'eau (in French), paper presented at 18th Congrès Association Français de Mécanique, Grenoble, France.

Benoit, M., F. Marcos, and F. Becq (1996), Development of a third generation shallow-water wave model with unstructured spatial meshing, paper presented at 25th International Conference on Coastal Engineering, pp. 465–478, Orlando, Fla., Am. Soc. Civil Eng., Reston, Va.

Bidlot, J., S. Abdalla, and P. Janssen (2005), A revised formulation for ocean wave dissipation in CY25R1, *Tech. Rep. Memo. R60.9/JB/0516*, Res. Dept., Eur. Cent. for Medium-Range Weather Forecasts, Reading, U. K.

Booij, N., R. C. Ris, and L. H. Holthuijsen (1999), A third-generation wave model for coastal regions 1. Model description and validation, *J. Geophys. Res.*, *104*(C4), 7649–7666.

Cavaleri, L., et al. (2007), Wave modelling—The state of the art, *Progr. Ocean.*, *75*, 603–674.

Donelan, M. A., J. Hamilton, and W. H. Hui (1985), Directional spectra of wind-generated waves, *Philos. Trans. R. Soc. London Ser. A*, *315*, 509–562.

Elfouhaily, T., B. Chapron, K. Katsaros, and D. Vandemark (1997), A unified directional spectrum for long and short wind-driven waves, *J. Geophys. Res.*, *102*(C7), 15,781–15,796.

Ewans, K. C. (1998), Observations of the directional spectrum of fetch-limited waves, *J. Phys. Oceanogr.*, *28*, 495–512.

Gelci, R., H. Cazalé, and J. Vassal (1957), Prévision de la houle. La méthode des densités spectroangulaires (in French), *Bull. Inf. Com. Oceanogr. Etud. Côtes*, *9*, 416–435.

Günther, H., S. Hasselmann, and P. A. E. M. Janssen (1992), The WAM model cycle 4 (revised version), *Tech. Rep. 4*, Deutsch. Klimatol. Rechenzentrum, Hamburg, Germany.

Hashimoto, N., H. Tsuruya, and Y. Nakagawa (1998), Numerical computations of the nonlinear energy transfer of gravity-wave spectra in finite water depths, *Coastal Eng. J.*, *40*, 23–40.

Hasselmann, D. E., M. Dunkel, and J. A. Ewing (1980), Directional wave spectra observed during JONSWAP 1973, *J. Phys. Oceanogr.*, *10*, 1264–1280.

Hasselmann, K. (1962), On the nonlinear energy transfer in a gravity wave spectrum. Part 1. General theory, *J. Fluid Mech.*, *12*, 481–500.

Hasselmann, K. (1974), On the spectral dissipation of ocean waves due to white capping, *Boundary Layer Meteorol.*, *6*, 107–127.

Hasselmann, K., et al. (1973), Measurements of wind-wave growth and swell decay during the Joint North Sea Wave Project (JONSWAP), *Dtsch. Hydrogh. Z. Suppl.*, *12*(A8), 1–95.

Hasselmann, S., and K. Hasselmann (1981), A symmetrical method of computing the nonlinear transfer in a gravity wave spectrum, *Hamb. Geophys. Einzelschr. Ser. A*, 52.

Hasselmann, S., K. Hasselmann, J. H. Allender, and T. P. Barnett (1985), Computations and parametrizations of the nonlinear energy transfer in a gravity-wave spectrum. Part II. Parameterizations of the nonlinear energy transfer for application in wave models, *J. Phys. Oceanogr.*, *15*, 1378–1391.

Hisaki, Y. (2007), Directional distribution of the short wave estimated from HF ocean radars, *J. Geophys. Res.*, *112*, C10014, doi:10.1029/2007JC004296.

Holthuijsen, L. H. (2007), *Waves in Oceanic and Coastal Waters*, 387 pp., Cambridge Univ. Press, Cambridge, U. K.

Hwang, P. H., D. W. Wang, E. J. Walsh, W. B. Krabill, and R. N. Swift (2000a), Airborne measurement of the wavenumber spectra of ocean surface waves. Part I: Spectral slope and dimensionless spectral coefficient, *J. Phys. Oceanogr.*, *30*, 2753–2767.

Hwang, P. H., D. W. Wang, E. J. Walsh, W. B. Krabill, and R. N. Swift (2000b), Airborne measurement of the wavenumber spectra of ocean surface waves. Part II: Directional distribution, *J. Phys. Oceanogr.*, *30*, 2768–2787.

Janssen, P. A. E. M. (1989), Wave-induced stress and the drag of air flow over sea waves, *J. Phys. Oceanogr.*, *19*, 745–754.

Janssen, P. A. E. M. (1991), Quasi-linear theory of wind-wave generation applied to wave forecasting, *J. Phys. Oceanogr.*, *21*, 1631–1642.

Janssen, P. A. E. M. (2004), *The Interaction of Ocean Waves and Wind*, 300 pp., Cambridge Univ. Press, New York.

Kahma, K. K. (1981), A study of the growth of the wave spectrum with fetch, *J. Phys. Oceanogr.*, *11*, 1503–1515.

Kitaigorodskii, S. A. (1983), On the theory of the equilibrium range in the spectrum of wind-generated gravity waves, *J. Phys. Oceanogr.*, *13*, 816–827.

Komatsu, K., and A. Masuda (1996), A new scheme of nonlinear energy transfer among wind waves: RIAM method—Algorithm and performance, *J. Oceanogr. Soc. Jpn.*, *52*, 509–537.

Komen, G. J., S. Hasselmann, and K. Hasselmann (1984), On the existence of a fully developed wind-sea spectrum, *J. Phys. Oceanogr.*, *14*, 1271–1285.

Komen, G. J., L. Cavaleri, M. Donelan, K. Hasselmann, S. Hasselmann, and P. A. E. M. Janssen (1994), *Dynamics and Modelling of Ocean Waves*, 532 pp., Cambridge Univ. Press, New York.

Korotkevich, A. O., A. N. Pushkarev, D. Resio, and V. E. Zakharov (2008), Numerical verification of the weak turbulent model for swell evolution, *Eur. J. Mech. B*, *27*, 361–387.

Kudryavtsev, V. N., V. K. Makin, and B. Chapron (1999), Coupled sea surface–atmosphere model 2. Spectrum of short wind waves, *J. Geophys. Res.*, *104*(C4), 7625–7639, doi:10.1029/1999JC900005.

Lavrenov, I. V. (2001), Effect of wind wave parameter fluctuation on the nonlinear spectrum evolution, *J. Phys. Oceanogr.*, *31*, 861–873.

Lavrenov, I. V. (2003), A numerical study of a non-stationary solution of the Hasselmann equation, *J. Phys. Oceanogr.*, *33*, 499–511.

Long, C., and D. Resio (2007), Wind wave spectral observations in Currituck Sound, North Carolina, *J. Geophys. Res.*, *112*, C05001, doi:10.1029/2006JC003835.

Longuet-Higgins, M. S., D. E. Cartwright, and N. D. Smith (1963), Observations of the directional spectrum of sea waves using the motions of a floating buoy, in *Ocean Wave Spectra, Proceedings of a Conference*, pp. 111–136, Prentice-Hall, Englewood Cliffs, N. J.

Masuda, A. (1980), Nonlinear energy transfer between wind waves, *J. Phys. Oceanogr.*, *10*, 2082–2093.

Mitsuyasu, H., F. Tasai, T. Suhara, S. Mizuno, M. Onkusu, T. Honda, and T. Rukiiski (1975), Observations of the directional spectrum of ocean waves using a cloverleaf buoy, *J. Phys. Oceanogr.*, *5*, 751–761.

Phillips, O. M. (1977), *The Dynamics of the Upper Ocean*, 2nd ed., Cambridge Univ. Press, Cambridge, U. K.

Phillips, O. M. (1985), Spectral and statistical properties of the equilibrium range in wind-generated gravity waves, *J. Fluid Mech.*, *156*, 505–531.

Polnikov, V. (1997), Nonlinear energy transfer through the spectrum of gravity waves for the finite depth case, *J. Phys. Oceanogr.*, *27*, 1481–1491.

Pushkarev, A. N., and V. E. Zakharov (2000), On conservation of the constants of motion in the models of nonlinear wave interaction, paper presented at *Sixth International Workshop on Wave Hindcasting and Forecasting*, pp. 456–469, Monterey, Calif., Joint Tech. Comm. for Oceangr. and Marine Meteorol.

Pushkarev, A. N., D. Resio, and V. E. Zakharov (2003), Weak turbulent theory of the wind-generated gravity sea waves, *Phys. D: Nonlinear Phenom.*, *184*, 29–63.

Resio, D. T., and W. Perrie (1991), A numerical study of nonlinear energy fluxes due to wave-wind interactions, part 1. Methodology and basic results, *J. Fluid Mech.*, *223*, 603–629.

Resio, D. T., and W. Perrie (2008), A two-scale approximation for efficient representation of nonlinear energy transfers in a wind wave spectrum. Part I: Theoretical development, *J. Phys. Oceanogr.*, *38*, 2801—2816.

Resio, D. T., J. Pihl, B. Tracy, and C. L. Vincent (2001), Nonlinear energy fluxes and the finite depth equilibrium range in wave spectra, *J. Geophys. Res.*, *106*(C4), 6985–7000.

Resio, D. T., C. E. Long, and C. L. Vincent (2004), Equilibrium-range constant in wind-generated wave spectra, *J. Geophys. Res.*, *109*, C01018, doi:10.1029/2003JC001788.

Snyder, R. L., F. W. Dobson, J. A. Elliot, and R. B. Long (1981), Array measurements of atmospheric pressure fluctuations above surface gravity waves, *J. Fluid Mech.*, *102*, 1–59.

Tanaka, M. (2001), Verification of Hasselmann's energy transfer among surface gravity waves by direct numerical simulations of primitive equations, *J. Fluid Mech.*, *444*, 199–221.

Toba, Y. (1973), Local balance in the air-sea boundary processes. III. On the spectrum of wind waves, *J. Oceanogr. Soc. Jpn.*, *29*, 209–220.

Tolman, H. L. (1991), A third generation model for wind on slowly varying, unsteady and inhomogeneous depth and currents, *J. Phys. Oceanogr.*, *21*, 766–781.

Tolman, H. L. (1992), Effects of numerics on the physics in a third-generation wind-wave model, *J. Phys. Oceanogr.*, *22*, 1095–1111.

Tolman, H. L. (2002), User manual and system documentation of WAVEWATCH-III version 2.22, *Tech. Rep. 222*, Natl. Weather Serv./Natl. Cent. for Environ. Prediction/Mar. Model. and Anal. Branch, NOAA, Silver Spring, Md.

Tolman, H. L. (2004), Inverse modeling of discrete interaction approximations for nonlinear interactions in wind waves, *Ocean Modell.*, *6*, 405–422.

Tolman, H. L., and D. Chalikov (1996), Source terms in a third-generation wind wave model, *J. Phys. Oceanogr.*, *26*, 2497–2518.

Trizna, D., R. Bogle, J. Moore, and C. Howe (1980), Observation by HF radar of the Phillips resonance mechanism for generation of wind waves, *J. Geophys. Res.*, *85*(C9), 4946–4956.

Van der Westhuysen, A. J. (2008), Advances in the spectral modelling of wind waves in the nearshore, Ph.D. thesis, Delft Univ. of Technol., The Netherlands.

Van der Westhuysen, A. J., M. Zijlema, and J. A. Battjes (2007), Nonlinear saturation-based whitecapping dissipation in SWAN for deep and shallow water, *Coastal Eng.*, *54*, 151–170.

Van Vledder, G. P. (2006), The WRT method for the computation of non-linear four-wave interactions in discrete spectral wave models, *Coastal Eng.*, *53*, 223–242.

Van Vledder, G. P., T. Herbers, R. Jensen, D. Resio, and B. Tracy (2000), Modelling of non-linear quadruplet wave-wave interactions in operational wave models, paper presented at 27th International Conference on Coastal Engineering, pp. 797–811, Sydney, Australia.

WAMDI Group (1988), The WAM model—A third generation ocean wave prediction model, *J. Phys. Oceanogr.*, *18*, 1775–1810.

Wang, D. W., and P. A. Hwang (2001), Evolution of the bimodal directional distribution of ocean waves, *J. Phys. Oceanogr.*, *31*, 1200–1221.

Webb, D. J. (1978), Non-linear transfers between sea waves, *Deep Sea Res.*, *25*, 279–298.

Yan, L. (1987), An improved wind input source term for third generation ocean wave modelling, *Tech. Rep. 8*, Royal Dutch Meteorol. Inst., De Bilt.

Young, I. R. (1994), On the measurement of directional wave spectra, *Appl. Ocean Res.*, *16*, 283–294.

Young, I. R. (1999), *Wind Generated Ocean Waves*, Elsevier, Amsterdam.

Young, I. R., and A. V. Babanin (2006), The form of the asymptotic depth-limited wind wave frequency spectrum., *J. Geophys. Res.*, *111*, C06031, doi:10.1029/2005JC003398.

Young, I. R., and G. Van Vledder (1993), A review of the central role of nonlinear interactions in wind-wave evolution, *Philos. Trans. R. Soc. London*, *342*, 505–524.

Young, I. R., L. A. Verhagen, and M. L. Banner (1995), A note on the bimodal directional spreading of fetch-limited wind waves, *J. Geophys. Res.*, *100*(C1), 773–778.

Zakharov, V. E. (1968), Stability of periodic waves of finite amplitude on the surface of a deep fluid, *J. Appl. Mech. Tech. Phys.*, *9*(2), 190–194.

Zakharov, V. E., and N. N. Filonenko (1966), Energy spectrum for stochastic oscillations of the surface of a fluid, *Sov. Phys. Dokl.*, *160*, 1292–1295.

Zakharov, V. E., and M. M. Zaslavsky (1982), The kinetic equation and Kolmogorov spectra in the weak-turbulence theory of wind waves, *Izv. Acad. Sci. USSR Atmos. Oceanic Phys., Engl. Transl.*, *18*, 747–753.

M. Benoit, Saint-Venant Laboratory for Hydraulics, c/o EDF R&D, 6 quai Watier, BP 49, F-78401 Chatou, France.

P. Forget, Laboratoire de Sondages Electromagnétiques de l'Environnement Terrestre, CNRS UMR 6017, Sud Toulon Var University, BP 132, F-83957 La Garde, France.

E. Gagnaire-Renou, EDF R&D, Laboratoire National d'Hydraulique et Environnement (LNHE), 6 quai Watier, BP 49, F-78401 Chatou, France. (elodie.gagnaire-renou@edf.fr)